Dust Obscuration in the Most Massive Galaxies of Epoch of Reionization

A Thesis

submitted to
Indian Institute of Science Education and Research Pune
in partial fulfillment of the requirements for the
BS-MS Dual Degree Programme

by

Prajnadipt Ghosh

Indian Institute of Science Education and Research Pune
Dr. Homi Bhabha Road,
Pashan, Pune 411008, INDIA.

May, 2023

Supervisor: Prof. Andrea Ferrara

Certificate

This is to certify that this dissertation entitled "Dust Obscuration in the Most Massive Galaxies of Epoch of Reionization" towards the partial fulfillment of the BS-MS dual degree programme at the Indian Institute of Science Education and Research, Pune represents study/work carried out by Prajnadipt Ghosh at Scuola Normale Superiore di Pisa under the supervision of Andrea Ferrara, Professor, Department of Physics at Scuola Normale Superiore di Pisa during the academic year 2022-23.

Prof. Andrea Ferrara

Committee:

Prof. Andrea Ferrara

Prof. Ramana Athreya

"when your hopes and dreams and goals are dashed, search among the wreckage, you may find a golden opportunity hidden in the ruins"

- Dr A.P.J Abdul Kalam, Wings of Fire

Declaration

I hereby declare that the matter embodied in the report entitled "Dust Obscuration in the Most Massive Galaxies of Epoch of Reionization" is the result of the work carried out by me at the Cosmology group in Scuola Normale Superiore di Pisa under the supervision of Prof. Andrea Ferrara and the same has not been submitted elsewhere for any other degree.

Prajnadipt Ghosh

Acknowledgments

I am deeply grateful to have had the opportunity to complete my MS thesis, and I would like to express my sincere appreciation to those who have supported and guided me throughout this journey.

First and foremost, I would like to thank my supervisor, Prof. Andrea Ferrara. and co-supervisor, Prof. Pratika Dayal, for their invaluable guidance, expertise, and unwavering support throughout my research. I would also like to thank my mentor Laura Sommovigo. Her mentorship, feedback, and encouragement were instrumental in shaping the direction of my work and pushing me to achieve my full potential. She has been a constant source of inspiration throughout my thesis.

I would like to express my heartfelt gratitude to my parents for providing unwavering moral and financial support throughout my academic journey, including the completion of my thesis. Their sacrifices and dedication towards my education have been indispensable in my success. Additionally, I would like to acknowledge the tremendous moral support that my friends have offered me during my time at IISER. In particular, I am grateful to Purva Parmar for his invaluable assistance in resolving coding-related queries.

Lastly, I am thankful to the research group at SNS Pisa for hosting me for six months and providing much-needed support while I was there. Special thanks to Tommaso Zana, Ivan Nikolic, David Prelogovic, and Sukalpa Kundu for their support in my research.

In conclusion, I would like to express my heartfelt thanks to everyone who has supported me throughout this journey. This thesis would not have been possible without their guidance, mentorship, and encouragement. Thank you all. Thank you, parents, teachers, and friends who have supported me.

Abstract

One of the biggest challenges in Cosmology is understanding the earliest galaxies formed in the Universe within one billion years of the Big Bang. This is a pressing issue because these galaxies are believed to be responsible for the last major cosmic phase transition, known as Cosmic Reionization, and for polluting the intergalactic medium with heavy elements. These processes significantly impact the subsequent formation of galaxies, governed by a complex network of physical processes collectively called "feedback."

Recent advancements in technology and the availability of powerful instruments such as the JWST and ALMA interferometer have enabled us to explore the depths of space and study these early galaxies in greater detail. With the help of JWST, we have observed galaxies beyond $z > 10$, while ALMA has provided insights into the properties of galaxies beyond $z > 7$.

Studies based on these new observations have discovered very bright sources at $z > 10$, which challenges the widely accepted model of large-scale structure formation known as the ΛCDM model. This raises questions about the physical processes involved in the rapid accumulation of large masses of these galaxies in a short period (around a few hundred million years after the Big Bang).

In this thesis, we propose a simple solution to this problem by postulating the role of "Dust Obscuration" in the observations. We use theoretical and numerical approaches to develop a model of UV and IR luminosity and Dust Obscuration. The dust produced in these early galaxies absorbs the UV radiation from young, hot, metal-free stars, resulting in lower UV luminosity than predicted by existing theoretical models. The dust then warms up and irradiates in the IR wavelength.

We propose a dust obscuration model that minimally affects the UV magnitude beyond $z \geq 10$. We also extend this model to the IR band using a simple chain rule transformation. However, we observe a slight disagreement between the model and the IR luminosity data, which we hypothesize could be due to the presence of "UV dark" galaxies. These galaxies do not emit UV radiation but contribute heavily to the IR wavelength. We propose the number density of these missing galaxies from the IR data.

List of Figures

Contents

Introduction

Understanding how galaxies formed and evolved is a fundamental question in cosmology. Despite extensive research in this field, the final frontier lies in piecing together the period of redshift interval 25 to 6, which occurred roughly 200 million to 1 billion years after the Big Bang. This period is critical because it witnessed two significant changes in the Universe. Firstly, stars began to form, emitting ultraviolet radiation from their hot, metal-free surfaces, marking the "cosmic dawn" period when dark matter halos capable of hosting star clusters or low-mass galaxies emerged. Secondly, the intergalactic medium transformed from a neutral and molecular gas to a fully ionized state, an event referred to as "cosmic reionization." Understanding these processes is crucial to developing a coherent picture of the evolution of galaxies.

Roughly 400,000 years after the Big Bang, the Universe's density began to decrease, causing a cooling effect that lowered the temperature to below 3000 K. This drop in temperature enabled ions and electrons to combine with neutral hydrogen and helium. Subsequently, photons were released from baryons, and the Universe became transparent, leaving behind the Cosmic Microwave Background Radiation (CMB) as a relic signature. This event led to a phase known as the "Dark Ages," during which the Universe was mostly dark.

Around 400 million years later, the "Dark Ages" came to an end with the emergence of the first galaxies emitting ionizing radiation. At first, the Intergalactic Medium (IGM) was mostly neutral, except in regions surrounding the first objects. As the reionization process progressed, a patchwork of neutral (HI) and ionized (HII) hydrogen formed and evolved. With the emergence of sufficient UV-emitting sources, the Universe's gas temperature and ionized fraction increased rapidly. Eventually, the ionized regions expanded and filled the entire Universe. Current limitations indicate that the epoch of reionization (EoR) took place between redshifts $z = 6 - 25$.

The epoch of reionization (EoR) represents a crucial juncture in the Universe's history. Prior to EoR, the formation and evolution of galaxies were primarily influenced by Dark Matter. However, during EoR, the impact of cosmic gas (baryonic matter) in galaxy evolution became more pronounced on a smaller scale, signifying a transition from one phase to the next.

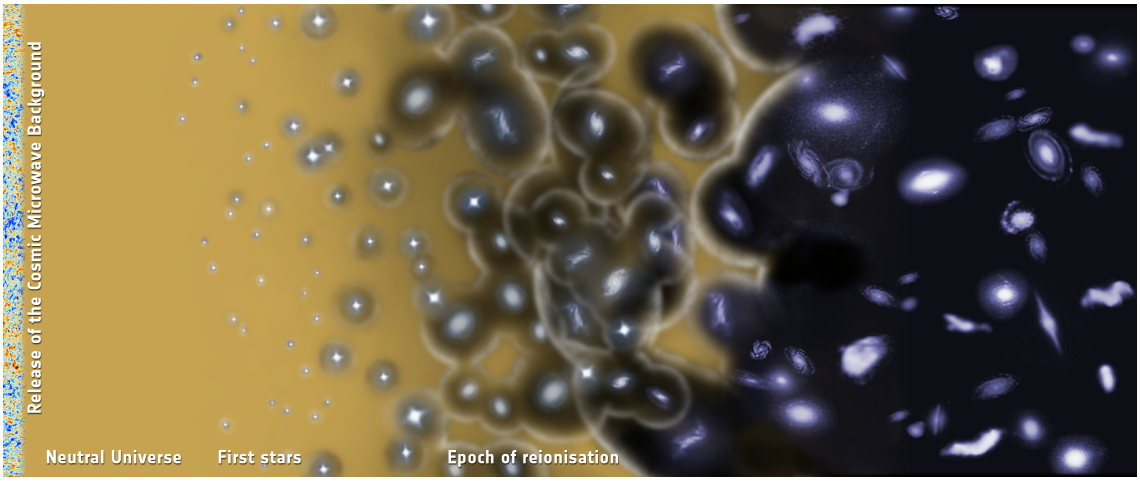

Figure 1: Image from European Space Agency website. This image illustrates the formation of early populations of star-forming galaxies and how they re-ionized the Universe. Baryonic gas gets attracted to assemble into DM halos, where it cools down and collapses to form the first stellar systems. UV radiation from these hot young stars photo-ionizes the neutral Hydrogen around, creating ionized bubbles. With the increase in the number of collapsed systems and ionized bubbles and their sizes, cosmic reionization is completed.

Studying galaxies and the intergalactic medium has numerous advantages. It enables us to pinpoint the time and complexity of transitions in the Universe and understand the physical processes that dictate the survival of primitive systems. These systems form the fundamental building blocks for the evolution of galaxies. The prevalence of low-mass systems in earlier times is linked to the assembly history of Dark Matter halos (Dayal and Dunlop 2014). Cold Dark Matter (CDM) is the preferred choice for large-scale structure formation, as warmer DM would delay early galaxy formation.

Recent advancements in technology and facilities have enabled us to obtain snapshots of the Universe at very early times. Sensitivity in near-IR observations from the Hubble Space Telescope (HST), mid-IR observations from Spitzer, and some rest UV spectroscopy from ground-based instruments provide us with critical physical insights into the early stages of star formation. HST's high spatial-resolution images reveal unobstructed star formation,

while Spitzer probes line emission and stellar population age in galaxies via the Balmer break. The Atacama Large Millimeter/submillimeter Array (ALMA) has contributed significantly to characterizing the physical properties of massive star-forming sources in the early Universe. It probes the reionization epoch using bright Interstellar medium (ISM) cooling lines, such as [C II] at 157.74 μm and [O III] at 88.36 μm, and simultaneously examines the far-IR dust continuum radiation, providing a measure of obscured star formation. The James Webb Space Telescope (JWST) has revolutionized this field by providing even more information, allowing us to explore spectroscopic redshifts up to $z > 7$.

The latest observations obtained from the James Webb Space Telescope (JWST) have challenged existing theories of galaxy formation and the ΛCDM model itself. The early-release Science programs (CEERS and GLASS) have discovered two very bright galaxies, GL-z13 and GL-z11, at very early epochs with stellar mass $M_* \approx 10^9 M_\odot$ and a luminosity of ($M_{UV} \approx -21$). These findings are in conflict with current models of galaxy formation. In addition to these bright galaxies, JWST has also discovered numerous other bright galaxies at earlier redshifts, whose joint abundance is 10 times larger than what is predicted by theoretical models. These observations confirm the tension between observations and theoretical predictions at the bright end of the Luminosity Function at $z \sim 7-9$, as reported by Bowler et al. 2020 [1] and Harikane et al. 2022 [2]. Thus, these new data have challenged existing theories and will require a re-evaluation of our current understanding of galaxy formation and evolution.

The inconsistency between the observed number of bright galaxies at high redshift and the predictions of the ΛCDM model may have several causes, such as an underestimation of the number of Dark Matter halos. However, astrophysical factors are more likely to be responsible, including a high conversion rate of gas into stars, a top-heavy initial mass function, or a high UV luminosity per unit of star formation. Another possibility is the presence of magnification bias. In this thesis, we propose a straightforward explanation: minimal dust obscuration beyond $z \geq 10$. Galaxies generate dust as a result of star formation, which can block their UV radiation and generate infrared radiation, leading to lower luminosities than predicted by theoretical models. To confirm this hypothesis, further studies of the infrared luminosity function are necessary.

This thesis is structured as follows. In Chapter 1, we lay the foundation for understanding the problem by discussing the physics of the formation and evolution of the universe and

the formation of structures. We also delve into the different stages of cosmic evolution and the ΛCDM framework for large scale structure formation in the universe. In Chapter 2, we explain the relevant quantities needed to comprehend the problem, such as the UV Luminosity Function, IR Luminosity Function, and dust. We also touch upon various research and observations done in these fields, as well as theoretical models and simulations.

In Chapter 3, we examine the issues uncovered by JWST in detail, particularly the inconsistencies between theoretical predictions and observational data, and explore potential causes for these discrepancies. Chapter 4 presents the minimal dust obscuration beyond $z \geq 10$ model of UV Luminosity Function and how it can be extended to the IR LF at $z = 7$. We provide an interpretation of the model and discuss its implications.

Finally, in Chapter 5, we conclude by summarizing the thesis and discussing its future scope. We highlight the importance of further research into the IR Luminosity Function to verify the proposed model and its potential impact on our understanding of galaxy formation and evolution.

Chapter 1

Cosmology: Big Bang to Present

Cosmology, also known as physical Cosmology, is the scientific study of the observable Universe's origin, evolution, and large-scale structures, including the laws of physics governing these areas. It is one of the oldest fields of Science and has been studied since ancient times. However, the modern history of galaxy formation began after Hubble's discovery of "Nebulae" in 1925, which helped to clarify that these objects were of extra-galactic origin and were named "Galaxies." Galaxies are composed of stars, stellar remnants, interstellar gas, dust, and dark matter, all held together by gravity. Since then, researchers have been on a quest to understand the physics behind galaxy formation.

Our understanding of the Universe has improved remarkably in the past two decades. The foundations of the Big Bang Standard model, Hubble expansion, the Cosmic Microwave Background (CMB), and the abundance of light elements have been strengthened. However, a few experimental pieces of evidence, such as a flat universe, the presence and abundance of dark matter particles, and accelerating Hubble expansion, require an exact theory to be explained. Nevertheless, with consistent efforts, researchers have developed a set of theorized stages of the evolution of the Universe.

This chapter aims to provide a context for the research that follows. Specifically, we will begin by explaining the stages of the evolution of the Universe. This would allow us to provide a foundation to discuss the ΛCDM model and its parameters. The ΛCDM model works as the standard parameterized Big Bang model, which explains the evolution of the Universe and the formation of galaxies via Large Scale Structure formation. We will briefly

look at these concepts to allow us to build a framework for understanding the challenges posed by the James Webb Space Telescope (JWST).

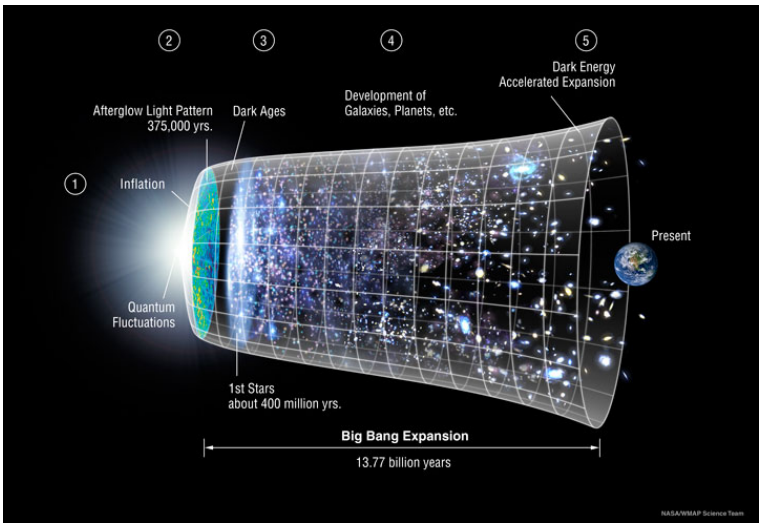

Figure 1.1: Image Credit: NASA/ LAMBDA Archive / WMAP Science Team: ΛCDM model of Cosmology. The above picture shows that the infant universe is an extremely hot, dense, nearly homogeneous mixture of photons and matter, tightly coupled as plasma.

1.1 Cosmic Evolution

In this section, the evolution of the Universe has been explained briefly. As shown in Fig. 1.2, the evolution can be explained as five different stages:

1. **Inflation:** Inflation is a phenomenon that occurred during the first 10^{-32} seconds after the Big Bang, where the universe underwent a rapid and exponential expansion, increasing its size by a factor of at least 10^{26}. This process is believed to have smoothed out irregularities and resulted in a uniform distribution of matter throughout the universe. Inflation also provides a possible explanation for two fundamental problems in cosmology - the flatness and horizon problems. The flatness problem refers to the unexpected flatness of the universe, given the initial conditions of the Big Bang. The horizon problem arises from the fact that distant regions of the universe appear to have had contact with each other, even though the light has not had enough time to travel between them. Inflation resolves both problems by allowing the universe to expand rapidly to a size that accounts for these observations.

2. **Recombination:** Recombination occurred around 380,000 years after the Big Bang (redshift $z \sim 1100$) and marked a significant stage in the evolution of the universe. During this time, the universe had cooled down enough for electrons and protons to combine, forming neutral atoms. This made the universe transparent, as photons could now travel freely without interacting with electrons. As these photons continued to travel through space, they eventually cooled down and became cosmic microwave background radiation (CMB), which can still be observed today. The CMB is considered to be one of the most important pieces of evidence for the Big Bang theory, as it is a remnant of the radiation that filled the universe in its early stages. The study of the CMB has provided important insights into the composition and properties of the universe and is a key tool in understanding the evolution of the universe.

3. **Galaxy Formation:** Galaxy formation is a significant stage in the evolution of the universe that began around 200 million years after the Big Bang ($z \sim 20-30$). During this stage, the density fluctuations in the universe caused by inflation led to the formation of the first structures, which are believed to have been small, dense regions of dark matter. As more dark matter accumulated in these regions, they attracted gas and dust through gravity, which formed the first galaxies. The process of galaxy formation was gradual, and it took billions of years for galaxies to evolve into the diverse shapes and sizes we observe today. The study of galaxy formation has revealed important information about the nature of dark matter, the role of black holes in galaxy evolution, and the mechanisms that drive star formation in galaxies. Understanding galaxy formation is essential to understanding the universe's evolution and the formation of the structures we observe today.

4. **Star Formation:** Star formation is a fundamental process in the evolution of the universe that occurs within galaxies. Stars are believed to form when dense regions of gas and dust within galaxies collapse under their own gravity. As the gas and dust in these regions become more concentrated, the temperature and pressure increase, eventually igniting nuclear fusion reactions that power the star. The process of star formation is complex and involves the interplay of many physical processes, such as turbulence, magnetic fields, and radiation feedback. Understanding star formation is crucial to understanding galaxies' properties and evolution, as stars are the building blocks of galaxies and play a critical role in the chemical and thermal evolution of the universe. The study of star formation has also led to important discoveries in

astrophysics, such as the existence of protostars, brown dwarfs, and planetary systems. Star formation began at a redshift of around 10, or about 400 million years after the Big Bang.

5. **Dark Energy Domination:** Dark energy domination refers to the current era of the evolution of the universe, where dark energy is the dominant component of the universe's energy density. Dark energy is a hypothetical form of energy that is believed to be responsible for the accelerated expansion of the universe. This acceleration was first observed in the late 1990s and has since been confirmed by numerous experiments and observations. Despite its name, dark energy is not well understood and is one of the greatest mysteries in modern physics. Its properties, such as its origin and composition, are still a subject of intense research and debate. The era of dark energy domination is characterized by the universe's continued expansion at an accelerating rate and the gradual fading away of structures, such as galaxies and galaxy clusters. It is expected that this era will continue indefinitely, leading to an increasingly dark and empty universe. The study of dark energy domination is crucial to our understanding of the fate and ultimate destiny of the universe. Dark energy domination began at a redshift of around 0.7, or about 5 billion years after the Big Bang and is ongoing.

1.2 ΛCDM Cosmology

The Lambda Cold Dark Matter (ΛCDM) model is a parameterization of the Big Bang Cosmological model. It proposes that the Universe comprises three major components: I) The cosmological constant Λ, which Einstein suggested to account for dark energy in his equation, II) Cold Dark Matter, and III) Ordinary Baryonic Matter. This simple model has successfully explained various properties of the cosmos, including the structure and existence of the Cosmic Microwave Background (CMB), the formation of large-scale structures of galaxies, and the observed abundances of Hydrogen, Helium, and Lithium. It also accounts for the accelerating expansion of the Universe. The model assumes that General Relativity is the correct theory of gravity on cosmological scales. Given the lack of a consensus on the energy density makeup of the Universe, the ΛCDM model emerged as the "concordance cosmology." It can be further developed by incorporating cosmological Inflation, quintessence, and other speculative and researched elements.

The ΛCDM model describes the expansion of the metric space that can be observed through the redshift of spectral lines in the light from distant galaxies and the time dilation in supernova luminosity curves. These phenomena occur due to the Doppler shift of electromagnetic radiation as it traverses through an expanding space. This expansion increases the distance between objects not influenced by gravity, yet it does not cause an increase in their size. Despite objects in close proximity having a relatively slower recession speed, those located farther apart can move away from each other at a velocity exceeding that of light due to an accumulation of expansion over great distances.

The ΛCDM model is made up of several components. Let's take a closer look at them one by one. Firstly, there's Λ, which represents the Cosmological Constant. Scientists believe it represents the energy present in empty space, which is also known as dark energy. Dark energy is thought to be responsible for the observed accelerating expansion of the Universe against the force of gravity. According to the theory of General Relativity, the cosmological constant has negative pressure, represented by the equation $p = -\rho c^2$. This pressure contributes to the stress-energy tensor, which causes the Universe to expand at an increasing rate. The dark energy, which is also represented by the symbol Ω_Λ, makes up a significant fraction of the total energy density of our Universe. The Dark Energy Survey, which used Type Ia Supernovae, estimated its value to be 0.669 ± 0.038 in 2018. Meanwhile, the PLANCK satellite data estimates it to be 0.6847 ± 0.0073, which is more than 68.3% of the total mass-energy density of the Universe.

Observations of gravitational effects like the rotation of galaxies, the bending of light by galaxy clusters, and the clustering of galaxies can't be explained by the amount of visible matter alone. To account for this, scientists have proposed the existence of Dark Matter. According to current hypotheses, Dark Matter is made up of non-baryonic Matter, which means it's not made of protons and neutrons. At the time of radiation-matter equality, Dark Matter particles had a velocity much lower than the speed of light, which is why they're referred to as "cold." These particles interact with each other and other particles through weak force and gravity, making them collisionless. Additionally, they can't be cooled through radiating photons, so they're considered dissipationless.

Dark Matter makes up approximately 26.5 % of the mass-energy density of the universe, while ordinary Matter accounts for the remaining 4.9 %. Ordinary Matter is composed of atoms, chemical elements, gases, and plasma that make up planets, stars, and galaxies.

However, the majority of Matter in the universe is invisible because less than 10 % of ordinary Matter is in the form of stars and gas found in galaxies. The Cosmic Microwave Background (CMB) and relic neutrinos make up a tiny fraction of the universe's energy density, only 0.01 % and 0.5%, respectively. However, these components played a significant role in the past, dominating the Matter at a redshift greater than 3200.

The ΛCDM model employs the Friedmann-Lemaitre-Robertson-Walker metric and the equations of state in cosmology to depict the current state of the observable universe starting from the inflationary period.

$$ds^2 = c^2dt^2 - a^2(t)\left(\frac{dR^2}{1-kR^2} + R^2d\theta^2 + R^2\sin^2\theta d\phi^2\right)$$

where c is the speed of light, R, r, θ, ϕ are co-moving coordinates, and $a(t)$ is the cosmic scale factor.k is the curvature of the universe, which can be positive, zero, and negative depending if the Universe is closed, flat or open respectively.

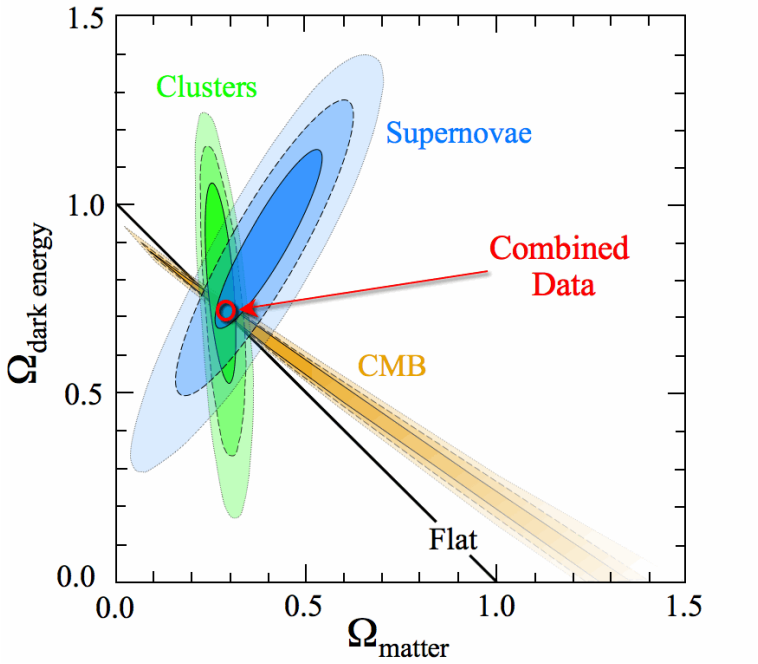

Figure 1.2: This plot gives the combined constraints to the cosmological densities Ω_Λ and Ω_M, using supernovae, CMB and cluster abundance data. The flat solid line represents $\Omega_\Lambda + \Omega_M = 1$[3]

1.2.1 Cosmic Expansion History

The expansion of the Universe is described using a dimensionless scale factor a, which represents the size of the universe at a given time. At the present time, t_0, the scale factor is set to 1. As the universe expands, the scale factor changes with time. The relationship between the scale factor and the observed redshift of light emitted at a certain time, $t_{\rm em}$, is given by:

$$a(t_{\rm em}) = \frac{1}{1+z}$$

Hubble parameter $H(t)$ describes the expansion rate as follows:

$$H(t) \equiv \frac{\dot{a}}{a}$$

where $\dot{a}$ is the time derivative of the scale factor. Using the first Friedmann equation we can calculate the expansion rate in terms of matter and radiation density ρ, the curvature k and the cosmological constant Λ

$$H^2 = \left(\frac{\dot{a}}{a}\right)^2 = \frac{8\pi G}{3}\rho - \frac{kc^2}{a^2} + \frac{\Lambda c^2}{3}$$

where c is the speed of light and G is the gravitational constant. Assuming $\rho_{\rm crit}$ as the critical present day density taking zero curvature k and cosmological constant Λ to be zero, we get:

$$\rho_{\rm crit} = \frac{3H_0^2}{8\pi G} = 1.878 \times 10^{-26} h^2 \ {\rm kg\ m^{-3}}$$

where $h \equiv H_0/(100\,{\rm km\ s^{-1}\ Mpc^{-1}})$ is the reduced Hubble constant. According to ΛCDM model, a positive cosmological constant predicts the Universe to expand forever regardless of the density.

The density parameter Ω_x for various species in present day is defined as a dimensionless

ratio:

$$\Omega_x \equiv \frac{\rho_x(t=t_0)}{\rho_{\rm crit}} \equiv \frac{8\pi G\rho_x(t=t_0)}{3H_0^2}$$

where x can be baryons (b), CDM (c), radiation (rad) and Dark Energy Λ. All these densities scale as different powers of a. Hence, we can rewrite the Friedmann equation as:

$$H(a) \equiv \frac{\dot{a}}{a} = H_0\sqrt{(\Omega_c+\Omega_b)a^{-3} + \Omega_{\rm rad}a^{-4} + \Omega_k a^{-2} + \Omega_\Lambda a^{-3(1+w)}}$$

Here, w refers to the equation of the state parameter of the Dark Energy. By construction, all the density parameters sum up to unity. The above relation is integrated to solve for the expansion history $a(t)$, and observable distance redshift relations are compared with the observations such as supernovae and baryon acoustic oscillations. In the minimal model, the Universe is assumed as flat and $w=-1$, hence,

$$\begin{aligned} H(a) &= H_0\sqrt{\Omega_m a^{-3} + \Omega_{\rm crit}a^{-4} + \Omega_\Lambda} \\ &= H_0\sqrt{\Omega_m(1+z)^3 + \Omega_{\rm crit}(1+z)^4 + \Omega_\Lambda} \end{aligned}$$

Observations predict $\Omega_{\rm rad} \sim 10^{-4}$, hence we can neglect the term. It has been noticed that the major contribution comes from Ω_m. Hence, we can approximately write the above equation as:

$$H(a) = H_0\sqrt{\Omega_m(1+z)^3 + \Omega_\Lambda}$$

Using PLANCK CMB data, the basic parameters are derived which are the important pillars of the ΛCDM model. These values are calculated using temperature-temperature (TT) spectra, temperature-E mode polarization (TE) spectra and the E mode-E mode polarization (EE) spectra. The best fit values calculated by these spectra as in Fig 1.3:

1. Hubble constant (H_0): The rate at which the universe is expanding at present. Value: $H_0 = 67.4 \pm 0.5$ km/s/Mpc (Planck 2018).

2. Baryon density ($\Omega_b h^2$): The fraction of the critical density made up of baryonic matter, where h is the Hubble constant in units of 100 km/s/Mpc. Value: $\Omega_b h^2 = 0.02237 \pm$

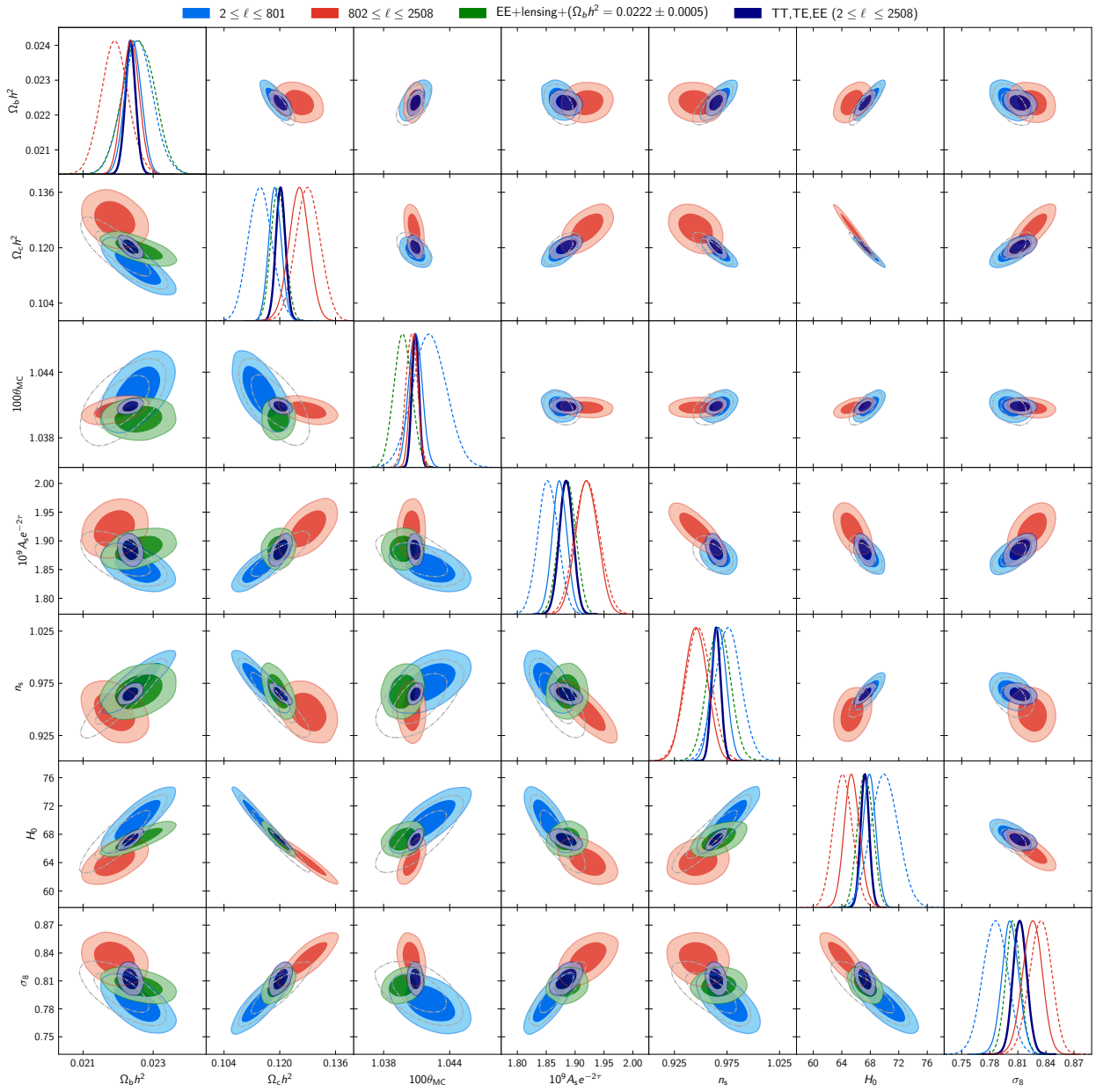

Figure 1.3: The base and derived ΛCDM parameter constraints from PLANCK data is shown in the above plot. These are 68% and 95% parameter constraint contours from the CMB power spectra.[4]

0.00015 (Planck 2018).

3. Cold dark matter density ($\Omega_{cdm}h^2$): The fraction of the critical density made up of cold dark matter. Value: $\Omega_{cdm}h^2 = 0.11933 \pm 0.00096$ (Planck 2018).

4. Spectral index of primordial perturbations (n_s): The scalar spectral index of the initial perturbations that seeded the large-scale structure of the universe. Value: $n_s = 0.965 \pm 0.004$ (Planck 2018).

5. Amplitude of primordial perturbations (A_s): The amplitude of the primordial power spectrum of density perturbations. Value: $\ln(10^{10} A_s) = 3.044 \pm 0.014$ (Planck 2018).

6. Dark energy density (Ω_Λ): The fraction of the critical density made up of dark energy. Value: $\Omega_\Lambda = 0.6844 \pm 0.0073$ (Planck 2018).

In addition to these, here are four extra parameters that are often included in more complex models:

1. Sound Horizon at last scattering $100\theta_{\rm MC}$: is the ratio of the sound horizon at the time of photon-baryon decoupling to the angular diameter distance to this same epoch. Value: $100\theta_{\rm MC} = 1.04090 \pm 0.00030$ (Planck 2018)

2. Root mean square mass fluctuations (σ_8): σ_8 is a parameter used in cosmology to describe the amplitude of density fluctuations in the universe on a scale of 8 mega-parsecs. Value: $\sigma_8 = 0.811 \pm 0.019$ (Planck 2018)

3. Curvature of the universe (Ω_k): The fraction of the critical density corresponding to spatial curvature. Value: $\Omega_k = 0.0007 \pm 0.0019$ (Planck 2018).

4. Reionization optical depth ($\tau_{\rm reio}$): The optical depth of the universe to electron scattering, which is related to the epoch of reionization of the intergalactic medium. Value: $\tau_{\rm reio} = 0.054 \pm 0.007$ (Planck 2018).

1.3 Large Scale Structure Formation

This section explains the origin of the universe's large-scale structure, like galaxies and clusters of galaxies, and how they develop in the later universe. Let us define density enhancement $\delta\rho$ and the density contrast $\Delta = \delta\rho/\rho$. When $\delta << 1$, these perturbations grow linearly. But, when this amplitude approaches unity, subsequent development becomes

non-linear, and they rapidly evolve into bound objects like galaxies and clusters of galaxies, where nonlinear astrophysical effects are important, such as star formation and feedback.

Let us define a joint probability of a given realization, $P[\delta(\mathbf{x}); t]$. This refers to the probability that at time t, the density at position $\mathbf{x_1}$ is $\bar{\rho}(t)[1 + \delta(\mathbf{x_2}), t]$ and so on. With increasing time, neighboring perturbations influence each other's growth through gravity. For earlier times, we can approximate perturbations to be independently evolving to each other. This can be shown in k-space in a better manner than in real space. Now, we can write the joint probability as a product of the probabilities of individual modes:

$$P[\delta(\mathbf{k}); t] \equiv P[\delta(\mathbf{k_1}), \delta(\mathbf{k_2}), ...; t)] \approx \prod g_k[\delta(k); t]$$

where g_k refers to the probability of a single mode having a specific amplitude and phase δ_k. At earlier times, we can think of δ_x as an uncorrelated random variable; hence central limit theorem motivates us to adopt a Gaussian distribution for g_k. A Gaussian random field has the property being solely defined by its mean and its variance:

$$\langle \delta_k \rangle = 0 \qquad \langle |\delta_k|^2 \rangle \equiv \sigma_k^2 \qquad \langle \delta_k \delta_p \rangle = 0 \qquad (\text{for k} \neq \text{p})$$

Analogously, probability of a location in real space ($\mathbf{x}$) having $\delta_x = q$ at time t is:

$$P[q] = \frac{1}{\sqrt{2\pi\Delta_x^2}} \exp\left(\frac{-q^2}{2\Delta_x^2}\right)$$

where the real space variance Δ_x^2 is written in terms of Fourier components:

$$\begin{aligned} \Delta_x^2 &\equiv \langle \delta_x^2 \rangle \\ &= V^{-2} \sum_{k,p} \langle \delta_k \delta_p^* \rangle e^{i(\mathbf{k}-\mathbf{p}).\mathbf{x}} \\ &= V^{-2} \sum_k \sigma_k^2 \end{aligned}$$

The discrete sum over the modes in the above equation can be converted to an integral by using the standard density of state relations. Let us assume $V = L^3$ is large enough to contain the representative volume of the Universe (beyond which the Universe is inhomogeneous); the $\mathbf{k} = \frac{2\pi}{L}\mathbf{n}$ boundary condition must be satisfied. This implies that $\mathbf{n} = (n_x, n_y, n_z)$ should

be integers 0,1,2... Hence density of states, $d^3k = \frac{(2\pi)^3}{V} d^3n$:

$$\sum_{\mathbf{k}} = \sum_{n} d^3n \implies \frac{V}{(2\pi)^3} \int d^3k$$

Using this, variance can be redefined as

$$\begin{aligned}
\Delta_x^2 \equiv \langle \delta_x^2 \rangle &= V^{-2} \sum_k \sigma_k^2 \\
&= \frac{V}{(2\pi)^3 V^2} \int \sigma_k^2 d^3k \\
&= \int_0^\infty \Delta_k^2 \frac{dk}{k}
\end{aligned}$$

The volume integral is performed assuming isotropy, and the term inside the integral is called "power per ln k" and is a representation of power spectra.

$$\Delta_k^2 \equiv \frac{V^{-1}}{2\pi^2} k^3 \sigma_k^2$$

We have expressed δ_x as a Gaussian random field above. If δ_x is a Gaussian random field, then they are also linear functions of δ_x. The excess mass in a sphere with radius R around a given point $\mathbf{x}$ is given by:

$$\delta M_R(\mathbf{x}) = \bar{\rho} \int_{|r| \leq R} \delta(\mathbf{x} + \mathbf{r}) d^3r$$

We simplify the above integral numerically by replacing the definite integral with an indefinite one by introducing **Window function** with the following properties:

$$W(\mathbf{r}) = \begin{cases} 1 \text{ if } |r| \leq R \\ 0 \text{ if } |r| > R \end{cases}$$

Using the window function, we can write the above integral over all space as:

$$\delta M_R(\mathbf{x}) \approx \bar{\rho} \int_V \delta(\mathbf{x} + \mathbf{r}) W(\mathbf{r}) d^3r$$

This equation is a convolution in real space. In k-space, it turns into multiplication

$$\delta M_R(\mathbf{k}) = \bar{\rho}\delta_k W_k^*$$

The average mass corresponding to this scale R is:

$$\bar{M_R} \equiv \bar{\rho} \int W(\mathbf{r}) d^3r \equiv V_W \bar{\rho}$$

where V_W is defined as the "effective volume" of the window function. Now the fractional excess or mass perturbation can be calculated on a scale of R. In k-space, it is given as:

$$\left(\frac{\delta M}{M}\right)_R(\mathbf{k}) = \frac{\rho\delta_k \bar{W}_k^*}{V_W \bar{\rho}} = \frac{\delta_k W_k^*}{V_W} \implies \left(\frac{\delta M}{M}\right)_R(\mathbf{x}) \equiv \delta_M = \frac{V}{(2\pi)^3} \int \left(\frac{\delta_k W_k^*}{V_W}\right) e^{i(k.x)} d^3k$$

Finally, we can write the variance in the mass field on a scale of R (**Mass Variance**):

$$\sigma_M^2(R) = \langle \delta_M^2 \rangle = \frac{1}{V_W^2} \int_0^\infty \Delta_k^2 W_k^2 \frac{dk}{k}$$

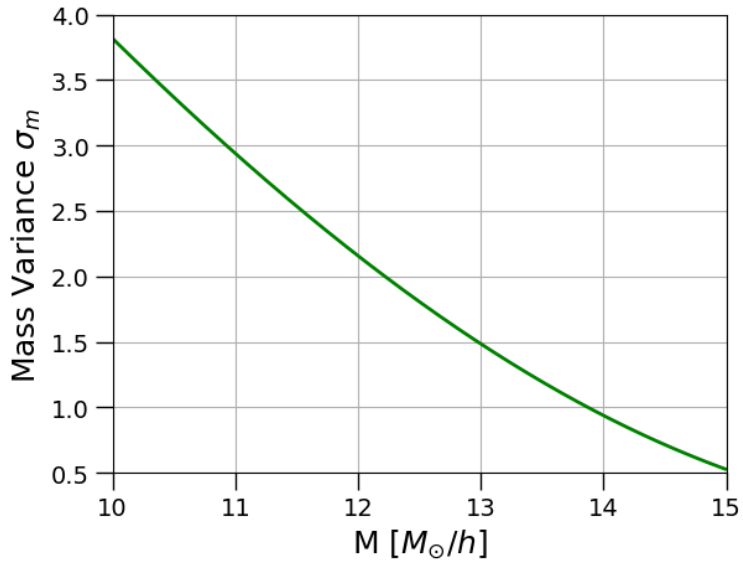

Figure 1.4: Mass Variance is the fundamental quantity required to define the collapse of halo mass.

Mass variance is a fundamental quantity for predicting the number density of collapsed structures(halos). The Window function defines the scale of interest over which matter power

spectrum integral is taken over. Mass variance is a Gaussian distributed quantity as it is constructed using a Gaussian distributed quantity δ_x. Hence, the probability of finding a mass fluctuation with amplitude between δ_M and $\delta_M + d\delta_M$ at a given scale R at redshift z is:

$$P(\delta_M, R, z)d\delta_M = \frac{1}{\sqrt{2\pi}\sigma_M} e^{-\frac{\delta_M^2}{2\sigma_M^2}} d\delta_M$$

There are various choices for the Window function for computing the mass variance: spherical top hat, the sharp k-space, and a Gaussian. Each window function has advantages and disadvantages. We commonly use the spherical top hat, as it is intuitive and clean in real space:

$$W(\mathbf{r}) = \begin{cases} 1 \text{ if } |r| \leq R \\ 0 \text{ if } |r| > R \end{cases} \quad W_k = 4\pi R^3 \left[\frac{sin(kR)}{(kR)^3} - \frac{cos(kR)}{(kR)^2} \right] \; V_W = \frac{4\pi}{3} R^3$$

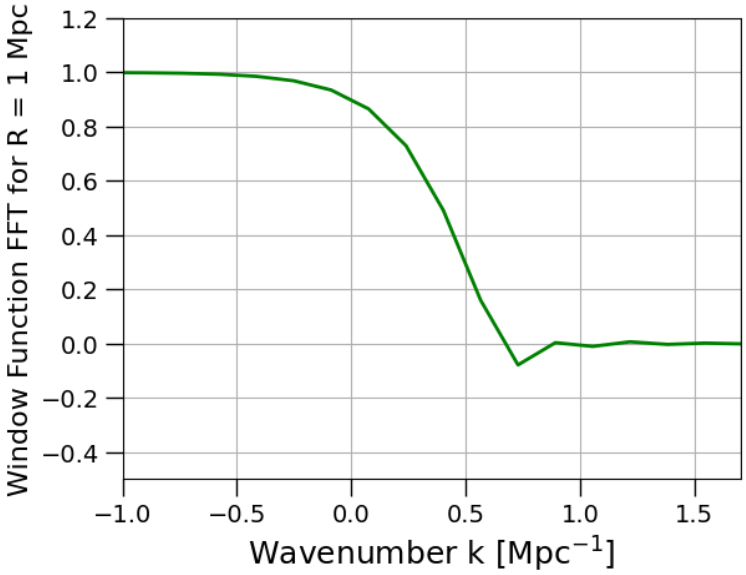

Figure 1.5: Spherical window function plotted at R = 1 Mpc. It is a smoothing tool on a scale of R. We can see that before k = 1, it returns the value of 1, and after that, it takes the function to 0.

One more important component of mass variance is the matter power spectrum, σ_k^2. It is an important fundamental concept of Cosmology. It describes the density contrast, i.e.,

the difference between local density and mean density, as a function of scale. It is usually expressed as (given by Eisenstein & Hu 1999)

$$\sigma_k^2 = Ak^n T^2(k) D^2(z,k)$$

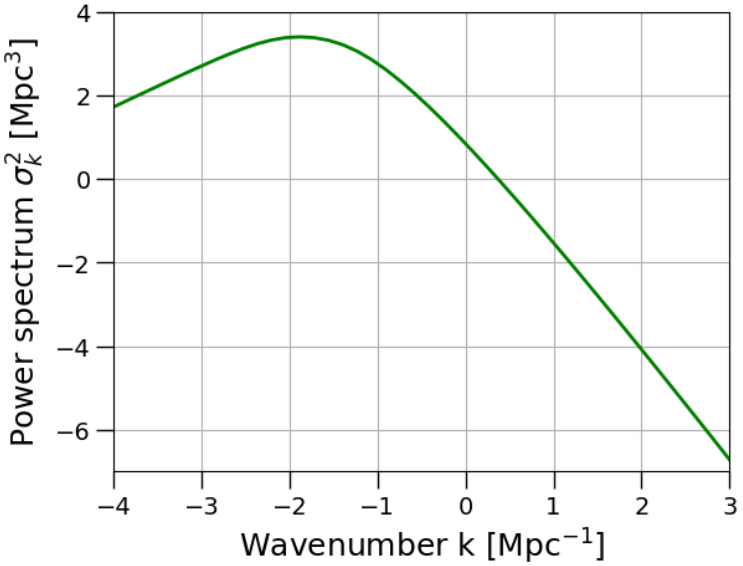

Figure 1.6: This plot represents the present day power spectrum assuming $\sigma_8 = 0.826$ and $h = 0.6775$

where A is a normalization constant normalized using present-day fluctuations on scales of $R = 8h^{-1}$ Mpc, computed with a spherical top-hat window function. As per Planck Collaboration XIII et al. 2016, $\sigma_M(z = 0, R = 8h^{-1}\text{Mpc}) = 0.82$. The second k^n term represents the primordial spectrum set by inflation represented by Power law. $T^2(k)$ is the transfer function, accounting for modifications of the primordial power spectrum on "small scales" due to processes at Matter-Radiation equality and Recombination. In this thesis, we will be using the transfer function given by Liddle et al. 1995 [5]:

$$T_{\text{CDM}}(q) = \frac{\ln(1+2.34q)}{2.34q} \times \left[1 + 3.89q + (16.1q)^2 + (5.46q)^3 + (6.71q)^4\right]^{-1/4}$$

Finally, $D(z,k)$ is the growth factor, describing the linear growth of perturbations, and is

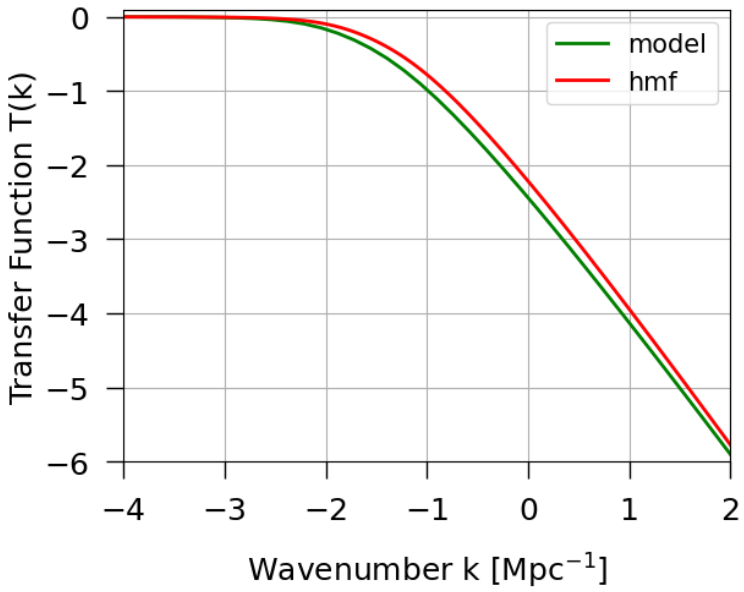

Figure 1.7: Transfer Function as proposed by Liddle et al. 1995, compared with simulations HMFCalc written by Steven Murray

normalized to be unity at z = 0:

$$D(z) = \frac{g(\Omega(z))}{g(\Omega_0)}\frac{1}{1+z} \qquad g(\Omega) = \frac{5}{2}\Omega\left[\frac{1}{70} + \frac{209\Omega}{140} - \frac{\Omega^2}{140} + \Omega^{4/7}\right]^{-1} \qquad \delta_c(z) = \frac{1.686}{D(z)}$$

1.3.1 Halo Mass Function

Halo mass function refers to the mass distribution of Dark Matter Halos; in other words, it gives us the number density of DM halos per mass at a given redshift z. We can evaluate the halo mass function using the tools explained in the last section. Let us define M_h to be the mass of collapsed structures (a halo) and $f_{\rm coll}(> M_h, z)$ to be the fraction of matter in the Universe contained inside halos of mass greater than M_h at the time z (collapsed fraction). Now, using the probability of mass fluctuation explained before; we can integrate it over the δ_M distribution we can calculate the collapse fraction.

$$f_{\rm coll}(> M_h, z) = \int_{\delta_c}^{\infty} P(\delta_M, R, z)d\delta_M = \frac{1}{\sqrt{2\pi}\sigma_M(R,z)}\int_{\delta_c=1.686}^{\infty} e^{-\frac{\delta_M^2}{2\sigma_M^2(R,z)}}d\delta_M$$

Here, δ_c is the critical density corresponding to the minimum overdensity of a collapsed halo. As we are dealing with a linear density field, we can use the result from the spherical collapse model where it's given that $\delta_c = 1.686$ for collapsed structures. We can perform these calculations on the overdensity field linearly extrapolated to $z = 0$. We can move the redshift dependence from σ_M by replacing $\delta_c(z) = 1.686/D(z)$:

$$f_{\rm coll}(> M_h, z) = \frac{1}{\sqrt{2\pi}\sigma_M(R)} \int_{\delta_c=1.686/D(z)}^{\infty} e^{-\frac{\delta_M^2}{2\sigma_M^2(R)}} d\delta_M$$

Let $\tau \equiv \delta_M/\sqrt{2\sigma_M^2}$ thus $d\tau = d\delta_M/\sqrt{2\sigma_M^2}$. So we can rewrite the above equation as:

$$\begin{aligned} f_{\rm coll}(> M_h, z) &= \frac{1}{\sqrt{\pi}} \int_{\delta_c/\sqrt{2\sigma_M^2}}^{\infty} e^{-\tau^2} d\tau \\ &= \frac{1}{2} \,{\rm erfc}\left[\frac{\delta_c(z)}{\sqrt{2}\sigma_M(R)}\right] \end{aligned}$$

But there is a problem with this formalism. As the matter field we have taken is discrete, we should recover the asymptotic limit $f_{\rm coll}(> M) \to 1$ as $M \to 0$. But our equation converges to 1/2. The missing factor of 2 is termed the "cloud in-cloud problem." We have not been accounting for Lagrangian regions, which, even if too underdense to be counted as belonging to a halo of mass M_1, still make up a part of a larger halo $M_2 > M_1$. So we should add one more term:

$$f_{\rm coll}(> M_h, z) = \int_{\delta_c}^{\infty} P(\delta_M, R, z) d\delta_M + \int_{-\infty}^{\delta_c} C(\delta_M, R, z) d\delta_M$$

The second term corresponds to the probability that a point with $\delta_M(R_1) < \delta_c$ will have $\delta_M(R_2) > \delta_c$. The "cloud in cloud" problem motivates a different perspective on the calculation of the halo mass function. Instead of using the above method, we can use the random walk (excursion set) method (in details in Appendix A). Since the δ_c barrier is a constant function of scale, we can cast the problem in terms of the classical stochastic diffusion equation. For every random walk trajectory which goes above the δ_c barrier at M_1, there is an equal probability that it will continue going above or continue going below δ_c for $M < M_1$. Hence the second term in the above equation has the same probability as the first term.

$$
\begin{aligned}
f_{\rm coll}(>M_h,z) &= \int_{\delta_c}^{\infty} P(\delta_M,R,z)d\delta_M + \int_{-\infty}^{\delta_c} C(\delta_M,R,z)d\delta_M \\
&= 2\times\int_{\delta_c}^{\infty} P(\delta_M,R,z)d\delta_M \\
&= 2\times\frac{1}{2}\,{\rm erfc}\left[\frac{\delta_c(z)}{\sqrt{2}\sigma_M(R)}\right] \\
&= {\rm erfc}\left[\frac{\delta_c(z)}{\sqrt{2}\sigma_M(R)}\right]
\end{aligned}
$$

When we differentiate the above equation with respect to mass, we obtain the halo mass function (Press and Schechter 1974 [6]):

$$
\frac{df_{\rm coll}(>M,z)}{dM} = \sqrt{\frac{2}{\pi}}\frac{\delta_c(z)}{\sigma_M^2(M)}\frac{d\sigma_M(M)}{dM}\exp\left[-\frac{\delta_c^2(z)}{2\sigma_M^2(M)}\right]
$$

The fraction of collapsed mass inside halos of mass around M is equal to their number of density times their mass divided by the average density of the universe, $df_{\rm coll} = (dN/dV)\times(M/\bar{\rho}) \equiv dn\times(M/\bar{\rho})$. So we can write the halo mass function in terms of the comoving number density of halos:

$$
\frac{dn(>M)}{dM} = \frac{\bar{\rho}}{M}\frac{df_{\rm coll}(>M,z)}{dM}
$$

It has been noticed that these analytic halo mass functions agree relatively well with results from N-body simulations, which follow the non-linear evolution of structure in detail. But it was also noted that they underestimated the abundance of massive halos and overestimated the abundance of small halos. So, an alternative form was suggested by Sheth & Tormen 1999 [7]:

$$
\frac{dn(>M,z)}{dM} = -\frac{\bar{\rho_0}}{M}\frac{\partial\ln\sigma_M}{\partial M}\sqrt{\frac{2}{\pi}}A\left(1+\frac{1}{\hat{\nu}^{2p}}\right)\hat{\nu}\exp\left[\hat{\nu}^2/2\right]
$$

with $\hat{\nu} \equiv \sqrt{a}\delta_c(z)/\sigma_M$. This form is motivated by the random walk procedure but by replacing the scale-independent barrier from spherical collapse, $\delta_c(z)$, with a scale-dependent

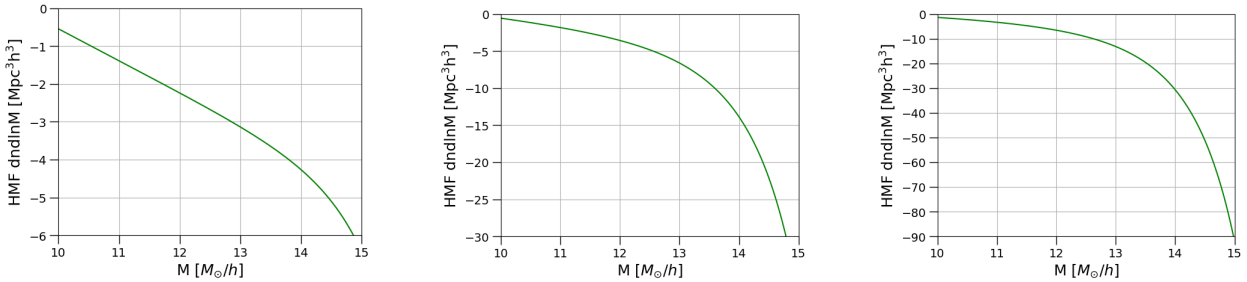

(a) $z = 0$ (b) $z = 4$ (c) $z = 7$

Figure 1.8: Halo Mass Function plotted, using Press Schechter Formalism, at various redshifts z = 0,4,7. The x-axis represents the mass of halos in the units of $M_\odot$ while the y-axis is the number density multiplied by M ($\frac{dn}{dlnM} = M \times \frac{dn}{dM}$). This gives the distribution of a number of halos of a certain mass at a certain redshift. We can observe that the plots are in accordance with the Binary Merger theory. According to this theory, smaller halos at higher redshifts merge to become bigger halos at smaller redshifts. Hence, as we can see from the plots, bigger halos $M = 10^{15}\, M_\odot$ are more abundant in lower redshifts as compared to higher redshifts.

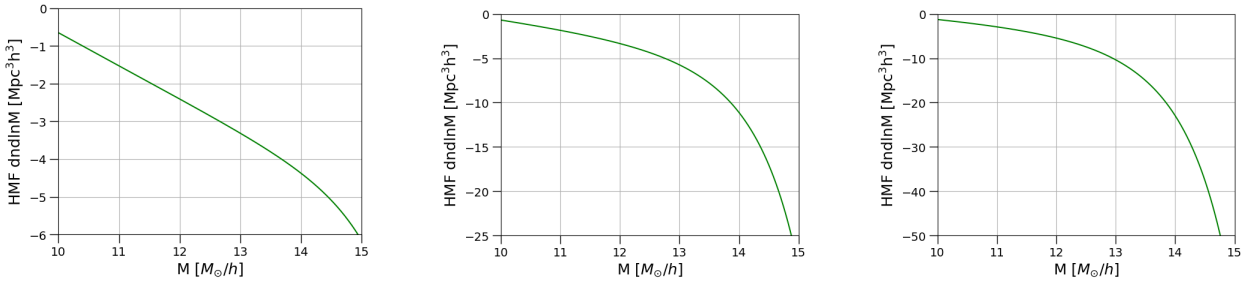

(a) $z = 0$ (b) $z = 4$ (c) $z = 7$

Figure 1.9: Halo Mass Function is plotted using Sheth Tormen formalism. It assumes ellipsoidal collapse rather than the spherical collapse of halos. In this formalism, we rectify the issue of overestimation of smaller and underestimation of bigger halos as compared to the Press Schechter halo mass function

barrier using an ellipsoidal collapse model:

$$\delta_c(M, z) = \sqrt{a}\delta_c(z)\left[1 + b\left(\frac{\sigma_M^2(M)}{a\delta_c^2(z)}\right)^c\right]$$

When fitted to the N-body simulation results, we obtain the constant values (Jenkins et al. 2001): $A = 0.353$, $p = 0.175$, $a = 0.707$, $b = 0.34$, $c = 0.81$. These mass functions are still widely used today, forming the basis for all early structure formation analytic studies.

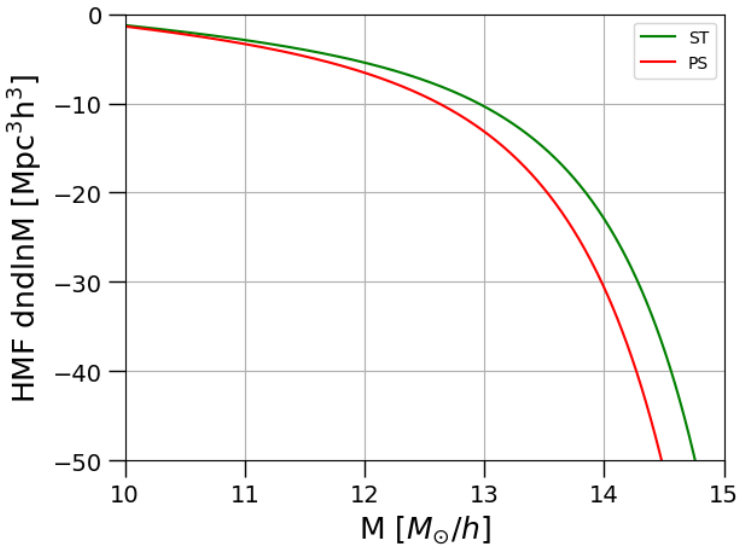

Figure 1.10: The green curve represents the HMF Plotted using Sheth and Tormen formula, while the red curve is for Press Schechter. We can clearly see that the PS method underestimates the number density of the bigger halos and overestimates the smaller ones.

Using the framework set by ΛCDM and the theory of large-scale structure formation, we move on to a more specific introduction to the concepts related to the thesis.

Chapter 2

Luminosity Functions and Effects of Dust

ΛCDM model parameterized the Big Bang model, and the large-scale structure formation explains galaxy formation analytically. With the development of various ground and space-based telescopes like PLANCK, SPITZER, HST, JWST, etc., we have been able to dig deep into the sky and detect galaxies. The galaxies, primarily composed of stars emit photons, which are detected by these telescopes. One of the important quantities measured by these telescopes is the flux. Using this flux, luminosity is calculated:

$$L = 4\pi d^2 \times \mathrm{f}$$

where f is the flux, L is the luminosity and d is the luminosity distance. Luminosity is the power output of a star. The net sum of these luminosities count as the luminosity of a galaxy. One of the important tools to study galaxies is the luminosity functions, which describe the brightness of galaxies at different wavelengths. Ultraviolet (UV) and infrared (IR) wavelengths are particularly useful for studying the properties of galaxies, as they probe different physical processes such as star formation, dust extinction, and the heating of interstellar dust by starlight. The UV and IR luminosity functions provide insights into the properties and evolution of galaxies at different epochs.

However, the presence of interstellar dust in galaxies can obscure our view of the under-

lying processes, affecting our measurements and interpretations of the luminosity functions. Therefore, understanding the properties of interstellar dust is crucial for accurate interpretation of the observations.

In this chapter, we will explore the basics of UV and IR luminosity functions and interstellar dust and their relevance in the study of galaxies. We will discuss the techniques used to measure these properties and the challenges involved in interpreting the data. Finally, we will highlight some of the recent advances in the field and their implications for our understanding of galaxy evolution.

2.1 UV Luminosity Function

The galaxies in the first $\sim$ 700 Myr from the Big Bang ($z > 8$) are mainly observed in the rest frame UV light. Considering the limited time since the Big Bang and the rapid growth of DM halos and stellar mass assembly at these early times, these galaxies are young and predominantly star-forming. As these galaxies are primarily made up of young stars, we have a galaxy spectrum of a power law function, and interstellar and intergalactic neutral gas absorbs photons that are bluer than the Lyman α wavelength. Hence we have a sharp spectral break at $\lambda \sim 0.12(1 + z)\ \mu m$. Therefore, the rest frame UV is the brightest area of the spectra. Due to HST, rest frame UV has been readily accessible for a large and deep area for source identification. Far-IR, including the [OIII] line observations and rest frame optical fluxes from Spitzer IRAC, has made follow-up observation possible for potential galaxy candidates.

UV Luminosity Function is one of the most fundamental quantities which can be extracted from the rest frame UV observations. UV LF is the density of UV sources per unit volume at a specific redshift. It is one of the most robust observables available for high-z galaxies. Many properties, such as the number of ionizing photons, cosmic star formation rate density history, dust properties at high redshifts, and connection between stellar mass and dark matter halo assembly, can be inferred from UVLF.[8] This section will use a theoretical approach to calculate the UV-LF and compare it with recent observations

In the simplest form, UV LF can be constructed by assigning each galaxy a cosmological ratio of baryons to DM (Ω_b/Ω_m) and then multiplying this with a constant star formation

efficiency ϵ_*. If feedback is assumed to be negligible, UV LF traces the same shape as the HMF. Hence, we can use the Schechter function to parameterize the UV-LF and obtain the number of galaxies as a function of Luminosity dn/dL. The Schechter function is a product of power law and exponential decay. Hence UV LF can be written in the following manner:

$$\frac{\mathrm{dn}}{\mathrm{dL}} = \phi(\mathrm{L}) = \frac{\phi_*}{L_*}\left(\frac{L}{L_*}\right)^{\alpha} \exp^{-(L/L_*)}$$

The UV LF can be described using three critical parameters from the above equation: I) ϕ_* - the characteristic number density, II) L_* is the characteristic luminosity, and III) α is the faint end slope. This function is a power law at the fainter, i.e., low luminosity end for $L < L_*$. After it crosses the knee/characteristic luminosity, it drops off exponentially. At high-z, most observables are defined using UV magnitude instead of luminosity. UV magnitude is determined such that:

$$\phi(\mathrm{M_{UV}})d(\mathrm{M_{UV}}) = \phi(\mathrm{L})d(-\mathrm{L})$$
$$\mathrm{M_{UV}} - \mathrm{M_{UV_*}} = -2.5\log\left(\frac{L}{L_*}\right)$$

Here M_{UV_*} is the characteristic (or knee) magnitude. Using these relations, we can write the Schechter function in the following ways:

$$\frac{\mathrm{dn}}{\mathrm{M_{UV}}} = \phi(\mathrm{M_{UV}}) = \frac{\ln 10}{2.5}\phi_* \left(10^{0.4(\mathrm{M_{UV_*}}-\mathrm{M_{UV}})}\right)^{\alpha+1} \exp^{10^{0.4(\mathrm{M_{UV_*}}-\mathrm{M_{UV}})}}$$

Recently, a combination of space-based surveys like HST and JWST and ground-based facilities like ALMA has made the construction of UV LF at high redshift possible. They have allowed us to map LF over eight magnitudes from $M_{\mathrm{UV}} \sim 14-23$ at $z \simeq 7$. It has been observed that the bright end at $z \simeq 7$ is better fitted by a double power law that steepens to the Schechter function by $z \simeq 5$ due to increasing dust extinction, AGN feedback and lensing magnification bias. It is important to note that three parameters of UV LF are degenerate.

For the reproduction of the bright end of UV-LF at $z \sim 5-10$, an increasing star formation efficiency needs to be added. Due to this, galaxies of the same luminosity reside in halos that are twice as massive at $z \simeq 5$ at $z \simeq 8$, which leads to steepening in the predicted faint end slope. Further addition of the Star formation efficiency function due to the feedback effects fine-tunes the theoretical UV LF.

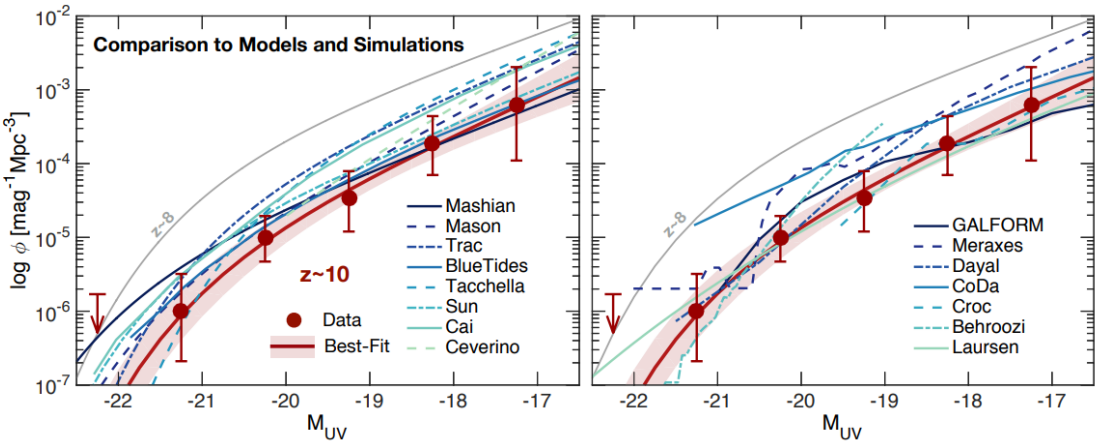

Figure 2.1: The figure presented here is adapted from Oesch et al. (2018), which compares the observed $z \sim 10$ UV luminosity function (LF), calculated in the paper using HST data to various models and simulations from the literature. The red line and dots represent the observational data from Oesch et al. (2018) [9], while the blue to green lines correspond to model LFs. All the models predict a considerable evolution in the UV LF between $z \sim 8-10$. However, the simulated UV LFs generally agree well with the observations and are mostly within the 1σ range.

UV luminosity function has been modeled in a variety of ways. Techniques such as abundance matching, semi-analytics, and hydro-dynamical simulations have predicted the UV LF to a reasonable agreement with the data. This is driven by numerous physical effects which have a degenerate effect on the UV-LF, such as SN and UVB feedback impact on the decreasing gas content of low-mass DM halos, the impact of dust on the observations of highly luminous galaxies, etc. Several observational biases have impacted the constraining of the faint end. These limitations have not allowed constraining the exact properties of the luminosity function.

Hubble Space Telescope and ground-based programs have been giving measurements of the redshift evolution of the LF's till $z \sim 8$. Bouwens et al. 2015, Atek et al. 2018, Bouwens et al. 2021, have constrained the Schechter function parameters to a good level. The shape of UV LF, if the observations are deep enough to detect the faint galaxies, does not deviate significantly from the Schechter function. Although a double power law has been suggested by Bowler et al. 2015 [10], Khusanova et al.[11] 2020, Harikane et al.[2] 2022, and Donnan et al. 2023 [12], for the highest redshift samples at $z \sim 6$. Before JWST, data indicated the presence of lesser luminous high redshift galaxies. With the release of JWST data, this field is looking toward big revolutionization. The early results like Naidu et al. 2022 [13],

Donnan et al. 2022 [12], and Finkelstein et al. 2022 [14], etc., have discovered more bright galaxies in the early universe at $z > 8$ than we expected. Various cosmological simulations have also been attempted to model high-z galaxies.

2.2 Dust

Interstellar dust is composed of tiny solid particles with sizes ranging from 0.01 to 0.1 micrometers. These particles are made up of various materials such as carbon, silicates, and metals and are found in the space between stars in galaxies. The origin of interstellar dust is not yet fully understood, but it is believed to be produced by processes such as supernovae, stellar winds, and collisions between dust grains.

The study of interstellar dust is significant as it offers insights into the physical and chemical processes that occur in space. The properties and behavior of dust grains can affect the observed properties of astronomical objects such as stars and galaxies. By studying the interaction of dust with light, astronomers can learn more about the composition and structure of the interstellar medium and the processes that shape it over time.

The thermal emission of interstellar dust grains has been observed at wavelengths longer than 100 micrometers, with the peak emission occurring at around 150 micrometers. Larger dust grains are in thermal equilibrium with the interstellar radiation field, meaning they have reached a balance between absorbing and emitting radiation. The heating of dust grains depends on the type of star that is nearby, with young and UV-luminous stars like OB-type stars heating the dust to higher temperatures than old and faint stars.

The process by which interstellar dust absorbs UV radiation and emits IR radiation is known as thermal emission. The energy absorbed by dust grains is transferred to the atoms and molecules within the grain, causing them to vibrate and rotate. This energy is then re-radiated by the dust grain as IR radiation, with the wavelength of the emitted radiation depending on the temperature of the dust grain. Hotter dust grains emit shorter-wavelength IR radiation, while cooler dust grains emit longer-wavelength IR radiation. The emission spectrum of a real emitter, such as dust grains, is modified from a blackbody using an emissivity term dependent on frequency. The value of the emissivity index β is thought to be related to the composition, size, and temperature of the dust grains and usually falls

within the range of 1-2 [15].

The dust in space significantly impacts the Spectral Energy Distribution (SED) of galaxies, affecting the reliability of SFR measurements. A young, dust-reddened stellar population can be misidentified as an older, dust-free one, making correcting the amount of dust attenuation to the observed flux essential. About half of the energy produced by galaxies is absorbed and reprocessed by dust formed as an end product of stellar evolution [16]. To recover the starlight hidden by dust, observations from FIR and sub-mm, where the dust emission peaks are, are necessary.

The thermal emission spectrum (S_ν) of a perfect emitter (blackbody) at a temperature T can be described by the Planck function:

$$B_\nu(T) = \frac{2h\nu^3}{c} \frac{1}{\exp(h\nu - k_B T) - 1}$$

where h is the Planck constant, ν is the frequency of emission, c is the speed of light, and k_B is the Boltzmann constant.

The emission spectrum of a real emitter (such as dust grains) is modified from a blackbody using an emissivity term:

$$S_\nu = Q_{em} B_\nu(T)$$

where Q_{em} is dependent on frequency:

$$Q_{em} \propto \lambda^{-\beta} \propto \nu^{\beta}$$

Hence, it is important for us to understand the properties of Interstellar dust and model it. This would also provide insights into physical and chemical processes that occur in space.

2.2.1 Modelling of Interstellar dust

There are numerous challenges in studying interstellar dust as they are difficult to observe directly. Indirect methods like absorption and scattering of light are employed to infer the properties of dust. There have been numerous attempted models of interstellar dust to explain its properties and dust. Modeling interstellar dust has turned out to be challenging because dust is a complex heterogeneous material that can vary in composition, size, and shape. The models need to take into consideration a wide range of physical and chemical processes, such as the heating and cooling of dust grains, the absorption and scattering of light, and chemical reactions that occur on the surfaces of dust grains.

Despite these challenges, several models of dust have been proposed over the years. These models explain the observed properties like size, composition, and optical properties of dust. One of the most widely used models of interstellar dust is the Draine & Lee 1984 model[17]. This model assumes the interstellar dust to be composed of a mixture of silicates and graphites and that the dust grains have a power law size distribution. This model has been successful in explaining the observed extinction curve in the Milky Way.

The model given by Weingartner & Draine 2001 [18] extends on the previous model to include aromatic hydrocarbons (PAHs), which are thought to be one of the important components of interstellar dust. This model has successfully explained the mid-IR emission features observed in many galaxies. There have been more complex size distribution models such as the one in Zubko et al. (2004) [19] model. It assumes the dust is composed of a mixture of silicates, graphites, and amorphous carbon grains. This has been used to explain the polarization properties of interstellar dust. The model given by Li & Draine [20] in 2001 assumes dust grains are fluffy aggregates of smaller subunits. This model has been used to explain the anomalous microwave emission observed in the Milky Way. [21]

2.2.2 Dust Attenuation

Assuming a complex geometric distribution, where light sources (stars) are distributed at varying depths regardless of the dust's nature, the resulting effect of dust is referred to as Dust Attenuation. The relative positioning between light sources and dust significantly affects light absorption and scattering. To account for dust attenuation, the radiative transfer

equation of light is described by an integrodifferential equation, which can be expressed for different wavelengths, such as UV and IR, as follows:

$$\frac{dI_\nu}{d\tau} = -I_\nu + \frac{a_\nu}{\pi} \int I_\nu \, \phi(\nu, \cos\Theta) \, d\Omega$$

Here, I_ν represents light intensity, τ is the optical depth through dust, a_ν is the dust albedo, $\phi(\nu, \cos\Theta)$ is the scattering phase function, and Θ is the angle between scattered photon and line of sight. For wavelengths where the source function is negligible, the first term on the right-hand side (RHS) describes the decrease in intensity of the original beam as it passes through dust, while the second term is the light added to the beam by scattering into the line of sight.

The solution to this equation is crucial in recreating the Spectral Energy Distributions (SEDs) of galaxies. For instance, in a simple scenario where a single point-like light source is obstructed by dust, the solution is:

$$\frac{dI_\nu}{d\tau} = -I_\nu \implies I_\nu = I_\nu^0 e^{-\tau}$$

This is a well-known solution for the extinction of a stellar spectrum caused by foreground dust, where I_ν^0 is the incident light, and τ_λ is the optical depth related to extinction curve $\kappa(\lambda)$ through the color excess $E(B-V)$.

The radiative transfer equation can be approximated by replacing the integral on the RHS with some central or mean value, turning it into a pure differential equation. For a homogeneous geometric distribution of dust and stars, the solution is:

$$I_\nu = I_\nu^0 \frac{1 - e^{-\tau'}}{\tau'}$$

Here, τ' is the effective optical depth that accounts for the average effects of scattering

into the line of sight.

2.3 IR Luminosity Function

Star formation Rate (SFR) is one of the essential quantities which entails information regarding the formation and evolution of galaxies. Stars are the fundamental building blocks of galaxies, and the rate of their formation impacts the structure, dynamics, and chemical composition of galaxies. Hence, SFR gives us insight into the physical processes that govern the formation and evolution of galaxies. One of the critical questions in Cosmology is, how did the star formation rate evolve with time, and how is it affected by factors such as properties of galaxies, intergalactic medium, etc.? Hence, star formation rate density (SFRD) is calculated to determine the amount of star formation in a given volume of space in a particular epoch. Our knowledge of SFRD at high redshifts is mainly based on UV rest frames. But, as we know, older galaxies produce dust that absorbs UV and emits IR; hence we are determining SFRD only on unobscured starlight.

Due to the discovery of Cosmic Infrared background at the end of the 1990s by the COBE satellite and deep extra-galactic surveys with Infrared Space Observatory (ISO) and the Submillimetre Common-User Bolometric Array (SCUBA), etc., there have been many searches to derive the star formation activity in the early universe which is obscured by dust. Such obscured dusty star-forming galaxies are called "Sub-millimetre galaxies" (SMGs). These galaxies are characterized by their IR Luminosities. Recently, ALMA has been the most powerful tool to study dust at high redshift. ALMA has shown that SMGs and other moderate star-forming galaxies contribute to the SFRD. Recent observations have indicated there could be more dust galaxies in the EoR than previously thought. This would directly impact the obscured Star Formation Rate density (SFRD). Hence, the shape and scale of IR LF are crucial to understanding the abundance of dusty galaxies and the time scale of dust production.

Theoretically, the IR Luminosity function is described by a double power law of the form:

$$\phi(\mathrm{L},\mathrm{z}) = \begin{cases} \phi_*(z)\left(\frac{L}{L_*(z)}\right)^{\alpha_{\mathrm{LF}}} \text{ if } \mathrm{L} < \mathrm{L}_*, \\ \\ \phi_*(z)\left(\frac{L}{L_*(z)}\right)^{\beta_{\mathrm{LF}}} \text{ if } \mathrm{L} \geq \mathrm{L}_* \end{cases}$$

Where α_{LF} and β_{LF} are the slopes at the faint and bright luminosities, respectively. L_* and ϕ_* are the characteristic galaxy luminosity and number density (as defined earlier) allowed to evolve with redshift. Previous works have shown that characteristic number density evolves as follows:

$$\phi_* \propto \begin{cases} (1+z)^{\psi_1} \text{ if } \mathrm{z} < \mathrm{z}_{\mathrm{turn}} \\ \\ (1+z)^{\psi_2} \text{ if } \mathrm{z} \geq \mathrm{z}_{\mathrm{turn}} \end{cases}$$

The observations put a constraint on the value of ψ_1 and the turnover redshift z_{turn}. ALMA large program Reionization Era Bright Emission Lines (REBELS) targets 42 galaxies at $z = 6.4 - 6.7$ with [CII] 158μm line scans. 16 of these galaxies exhibit dust detection, of which 15 have been spectroscopically confirmed. Based on this data, Barrufet et al. 2023 predict one of the first observational IR LF in EoR based on a UV-selected galaxy sample. The IR LF estimates are well reproduced by a Schechter function with a characteristic luminosity of $\log\left(L_*/L_\odot\right) = 11.6^{+0.2}_{-0.1}$ at $z \sim 7$. The evolution of the faint end of the infrared LF has been sampled by Gruppioni et al. 2020 [22] using the ALMA blind survey, ALPINE, in the redshift range of $z \simeq 2 - 6$. Zavala et al. 2021 [23] have compiled results from various surveys and combined them with semi-empirical modeling to constrain the evolution from $z > 5$.

In summary, the current measurements of the IR LF rely on a few dusty sources at $z > 3.5$, leading to large uncertainties in the IR LF parameters and hence disagreement between various survey results.

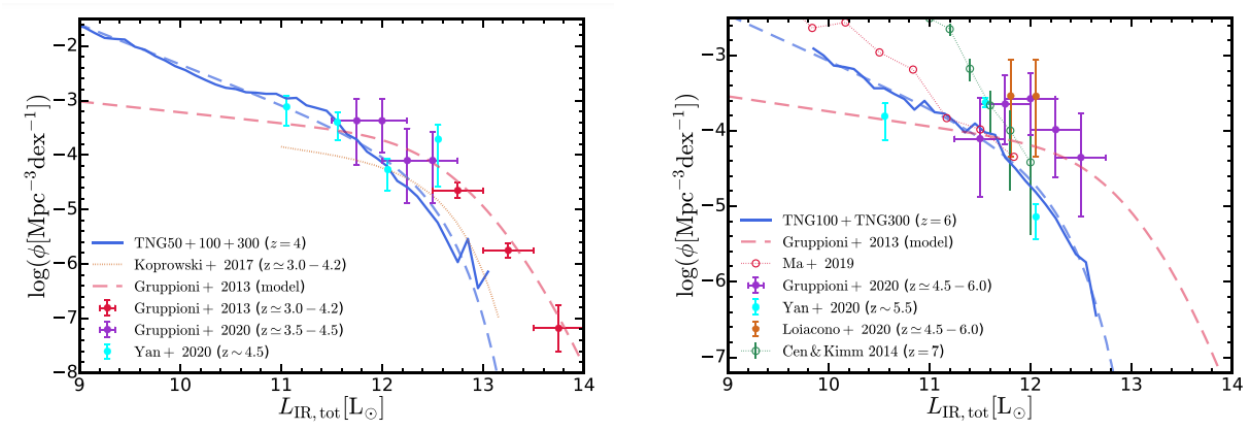

Figure 2.2: The figure presented in Xhen et al. (2022) [24] shows a comparison of various models, observations, and simulations for the bolometric infrared (IR) luminosity function (LF) at redshifts $z = 4$ and $z = 6$. The solid lines correspond to the IllustrisTNG simulations, while the solid markers represent observational data, and the dashed line shows that Schechter fits the observations. Theoretical works are depicted with open markers and dotted lines.

Chapter 3

New Telescope, New Challenges

The formation and evolution process of gravitationally bound structures, such as galaxies, has been explained through ΛCDM cosmology. Hierarchical models of galaxy formation, based on the standard ΛCDM model, have effectively predicted the properties and evolution of galaxies across different redshifts. Theoretical approaches, including numerical simulations and semi-analytical models, have played a crucial role in studying the assembly, composition, and kinematics of early galaxies, along with their relation to reionization. However, these models' validity must be tested and established through observational data.

Observational data from sources like Hubble Space Telescope (HST), Spitzer, and ground-based telescopes have significantly contributed to our statistical knowledge of the Epoch of Reionization ($z > 6$). The UV Luminosity Functions obtained from these sources have been reliably determined up to $z \simeq 9$ (Bouwens et al. 2021)[25]. These observations have enabled the derivation of other crucial quantities, such as Cosmic Stellar Mass Density and Star Formation Rate Density (SFRD). Further observations by the Atacama Large Millimeter Array (ALMA) have revealed the impact of dust extinction on the LF and SFRD determinations, especially at the highest masses, through the ALMA REBELS program.

3.1 Blue Monsters?

The advent of the James Webb Space Telescope (JWST) has brought about a revolutionary change in the field of observation, challenging existing theoretical predictions. At unprecedentedly high redshifts ($z > 10$), JWST has detected numerous bright ($M_{\rm UV} \sim -21$), massive, and blue galaxy candidates, including around 20 sources at $z > 11$, some with an incredibly high brightness of $M_{\rm UV} \leq -23$. The existence of these "blue monsters" (Ziparo et al. 2023[26]) challenges the predictions of standard theoretical models.

The new data from JWST has allowed for the study of luminosity functions (LFs) up to $z \simeq 14$, which has revealed a minimal evolution of the bright end of the UV LF between $z = 7 - 14$. However, these results do not correspond with the extrapolated $z \simeq 7$ LF is given by Bouwens et al. 2016, which predicts a sharp drop in the number density of sources at $M_{\rm UV} \leq -21$. This discrepancy can be resolved through two hypotheses: a much higher star formation efficiency concerning lower-z systems or the unattenuated nature of galaxies at $z > 10$ due to a drastic drop in dust optical depth.

Most sources observed at $z \geq 10$ exhibit a high blue UV slope, supporting the hypothesis of minimal obscuration. However, from high stellar mass, a consistently high dust content is expected, while extremely low dust optical depth implies very low dust content or attenuation. Moreover, while SED fitting analysis of 15 gravitationally lensed $z = 10 - 16$ galaxies reveals an upper limit of dust attenuation of $A_{\rm V} < 0.02$, JWST data points in the opposite direction by detecting galaxies with blue but not ultra-blue UV spectral slopes and low (but not primordial) metallicities.

3.2 Non-Allergic Dusty Galaxies

The formation of the first galaxies and their mass buildup remains a critical question in astrophysics. Recent discoveries of high-redshift galaxies have expanded our knowledge, including the detection of numerous luminous and massive sources at $z > 9$, which raises questions about the pace of early stellar mass production. However, major observations have been in rest-frame UV, which is not entirely reliable due to dust absorption. This means that highly star-forming galaxies obscured by dust could be missed.

ALMA has become the most potent tool for studying dust at high-z, bridging the gap between extremely dusty massive galaxies and more moderate star-forming galaxies. Recent observations have enabled the discovery of high-z dust galaxies at $z > 6$. Fudamoto et al. 2021 serendipitously detected two dusty galaxies at $z \sim 7$, implying the presence of more dusty galaxies in the Epoch of Reionization (EoR) than previously theorized. The presence of these galaxies would significantly impact obscured SFRD estimates. However, there are differing conclusions on SFRD based on serendipitous sources. To alleviate this problem, measuring the IR Luminosity Function is crucial. The shape and scale of the IR LF are essential to understanding the abundance of dusty galaxies and the rapidity of dust formation, which would directly affect the obscured sources' SFR.

Chapter 4

A New Model

The previous chapter highlighted the James Webb Space Telescope (JWST) discovery of an unexpectedly high number of galaxies that exhibit high luminosity at high redshifts. This phenomenon has prompted various explanations, including an increased halo density compared to that predicted by the ΛCDM model, as well as astrophysical mechanisms such as an enhanced gas-to-stars conversion rate at high redshifts, a top-heavy IMF, amplified UV luminosity per unit mass of stars formed, and the effects of magnification bias, including weak and strong lensing, on galaxy detection.

This chapter presents a simplified explanation for the observed phenomena: the virtual absence of dust obscuration beyond $z \geq 11$. We propose a dust obscuration model that disappears at higher redshifts to account for the observed absolute UV magnitude for $z \leq 11$. Using this model, we extrapolate the infrared luminosity function (LF) to explain the abundance of dusty galaxies recently discovered in ALMA REBELS and ALPINE observations.

4.1 UV LF with dust attenuation

The purpose of this section is to construct a concise and straightforward physical model to account for the redshift evolution of the UV Luminosity function, $\phi(M_{\rm UV})$. This model draws inspiration from Ferrara et al.'s work in 2022,[27], which motivates the approach adopted in this thesis. However, we take the initiative to modify and expand upon the original model

to suit our research objectives better.

Given the ΛCDM model, we can assume that a galaxy of stellar mass M_* is hosted by a dark matter (DM) halo with mass M_h. We assign each galaxy a cosmological ratio of baryons to the DM and multiply it with a constant star formation efficiency, ϵ_*,

$$M_* = \epsilon_* \left(\frac{\Omega_b}{\Omega_m} \right) M_h$$

The star formation timescale is assumed to be the free fall time of gas into dark matter halos, expressed as $t_{\rm ff} = (4\pi G\rho)^{-1/2}$, where ρ represents the average gas density within virialized structures, given by $\rho = 18\pi^2\langle\rho\rangle$. The value of $\langle\rho\rangle$ is determined by the average cosmic density at redshift z, defined as $\langle\rho\rangle = \Omega_b(1+z)^3\rho_{cr}$. We can express $t_{\rm ff}$ as $\zeta H(z)^{-1}$, where $\zeta = 0.06$ and $H(z)^{-1}$ denotes the Hubble time at redshift z. Hence, we can derive the star formation rate (SFR) using the following equation:

$$\begin{aligned}
\dot{M}_* &= \frac{M_*}{t_{\rm ff}} \\
&= \left(\frac{\epsilon_*}{\zeta} \right) \left(\frac{\Omega_b}{\Omega_m} \right) H_0 E(z) M_h \\
&= 22.7 \left(\frac{\epsilon_*}{0.01} \right) \left(\frac{1+z}{8} \right)^{3/2} \frac{M_h}{10^{12}} \\
&= 22.7 \left(\frac{\epsilon_*}{0.01} \right) \left(\frac{1+z}{8} \right)^{3/2} M_{12} \qquad\qquad \left(M_{12} = \frac{M_h}{10^{12}} \right)
\end{aligned}$$

The rest-frame UV 1500 Å luminosity, denoted as $L_{\rm UV}$, serves as a reliable indicator of the star formation rate (SFR) in high-redshift galaxies, provided that the star formation rate occurs over a timescale longer than 100 million years (Kennicutt 1998 [28], Madau and Dickinson 2014 [29]) and accounting for dust attenuation. The dust-corrected SFR of a galaxy is directly proportional to its rest-frame UV continuum luminosity, with the constant of proportionality represented by $K_{\rm UV}$ [30].

$$L_{\mathrm{UV}} = \frac{\dot{M}_*}{K_{\mathrm{UV}}} = \frac{\dot{M}_*}{1.703 \times 10^{-10}}$$

The constant of proportionality, K_{UV}, is expressed in units of $M_\odot : \mathrm{yr}^{-1} : /L_\odot$. The value of K_{UV} is determined according to Bouwens et al. (2022) [25], whose findings will be utilized to compare the model.

In order to construct a model for the evolution of the bright end of the Luminosity function, we take into account the effects of Supernova (SN) feedback. Specifically, in smaller galaxies hosted by smaller halos, the expulsion of star-forming gas by feedback leads to a quenching of star formation and, thus, a reduction in the efficiency factor ϵ_*. The physical form of the model is inspired by Dayal et al. (2014)[31](in details in Appendix B):

$$\epsilon_* = \epsilon_0 \frac{v_c^2}{v_c^2 + f_w v_s^2}$$

where $\epsilon_0 = 0.02$ and $v_c(M)$ is the halo circular velocity defined as:

$$v_c(M) = 23.4 \left(\frac{M}{10^8}\right)^{1/3} \left(\frac{1+z}{10}\right)^{1/2}$$

The energy coupling efficiency of supernova explosions with the gas is denoted by $f_w = 0.1$, and the characteristic velocity associated with the supernova energy per unit stellar mass formed is given by $v_s = \sqrt{\nu E_0} = 975\,\mathrm{km\,s^{-1}}$. These values are calculated specifically for a Salpeter initial mass function ranging from 1 to 100 $M_\odot$. To maintain consistency with local galaxies, we set ϵ_0 to 0.02, following Krumholz (2017)[32].

The UV luminosity can be converted into absolute magnitude M_{UV} using the relation given by Oke and Gunn 1983 [33]:

$$M_{\rm UV} = -2.5 \log_{10}(L_{\rm UV}) + 5.89$$

To include the effect of dust attenuation in the luminosity of galaxies, we propose the following relation for conversion:

$$\boxed{\rm M_{UV} = -2.5 \log_{10}(L_{\rm UV}) + 5.89 + 1.087\tau_{\rm eff}}$$

The last term accounts for attenuation, quantified by the effective optical depth at 1500 Å, $\tau_{\rm eff}$. We need to note that the physical value of optical depth τ_λ is different from $\tau_{\rm eff}$, as the latter involves the effects of radiative transfer. In this model, we do not make predictions about dust attenuation. We use ALMA REBELS data, which showed that $\tau_{\rm eff}$ is proportional to SFR. We find the functional form by setting two conditions:

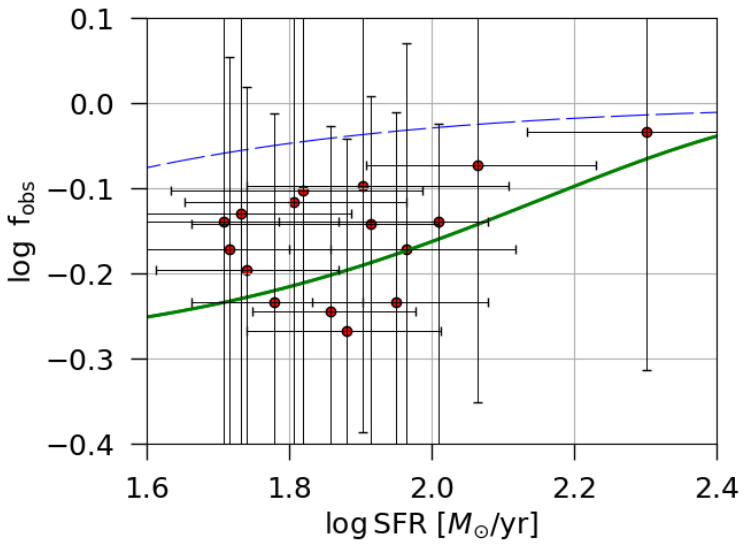

Figure 4.1: This plot represents the evolution of f_{obs} as a function of SFR. As the SFR increases, the amount of radiation obscured increases, indicating more dust obscuration in these galaxies, hence observing lesser UV magnitude. The plot for f_{obs} (green) perfectly fits the Bouwens et al. 2021 $z = 7$ points. The blue curve shows the fit for low redshift $z = 2.5$ from Whitaker et al. 2017.

1. it best fits the luminosity function at $z = 7$

2. it is consistent with obscured SFR function

$$f_{\rm obs} = \frac{\rm SFR_{IR}}{\rm SFR_{IR} + SFR_{UV}} = 1 - \exp(-\tau_{\rm eff})$$

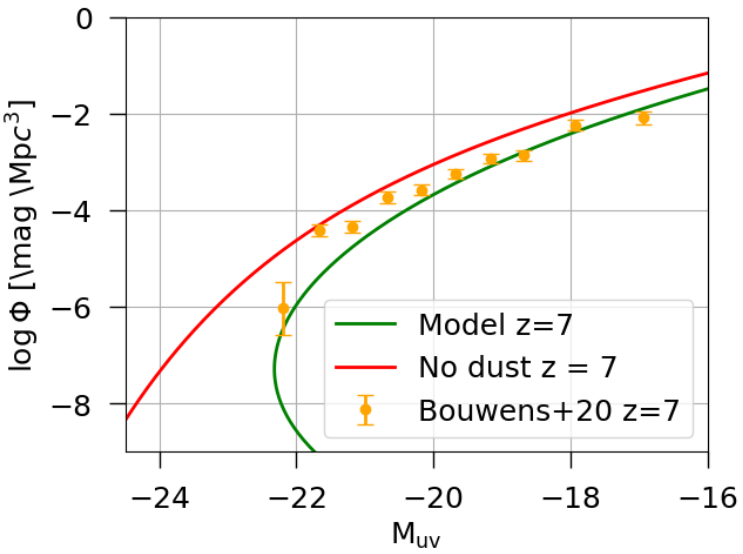

Figure 4.2: The plot's x-axis displays the calculated $\rm M_{UV}$ magnitude of the model, with brighter galaxies having more negative UV magnitudes and being larger. The y-axis shows the UV Luminosity function, with the green curve representing the model that incorporates the added dust obscuration term, while the red curve represents a model with no dust ($\tau_{\rm eff} = 0$). The data points are sourced from Bouwens+21 data. The plot indicates that the model in consideration, with the added dust obscuration term, is in complete agreement with the data observed by ALMA REBELS.

Using this procedure on REBELS data, we get the following relation:

$$\tau_{\rm eff} = 0.7 + 0.0164 \left(\frac{\rm SFR}{10\ M_\odot\ yr^{-1}} \right)^{1.45}$$

Motivated by the fact that a simple UV LF traces the Halo Mass function, a chain rule can be employed to move from HMF to UV LF in the following manner:

$$\phi(M_{\rm UV}) = \frac{dn}{dM_h} \frac{dM_h}{dM_{\rm UV}}$$

4.2 Model IR Luminosity

Our model extends beyond the UV Luminosity function to calculate the IR Luminosity function using semi-analytical methods. This involves understanding how dust interacts with light. When dust particles encounter UV photons, which have wavelengths similar to the size of the dust particles, they absorb the photons' energy. This causes the dust particles to vibrate and rotate, leading to heating. The heated dust particles then emit radiation in the electromagnetic spectrum's infrared (IR) part. The wavelength of the emitted radiation depends on the temperature of the dust particles: warmer dust emits shorter wavelengths (closer to the visible range), while cooler dust emits longer wavelengths (closer to the radio range). This process is known as blackbody radiation and is a fundamental principle in physics. As a result, IR emission is a crucial indicator of dust heating and can reveal necessary information about star formation activity in galaxies. [21]

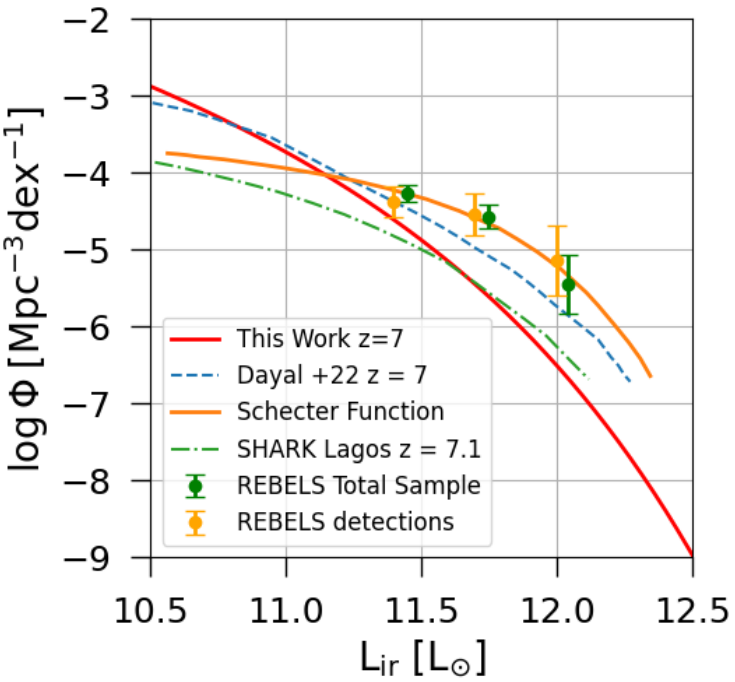

Figure 4.3: The plot depicts the IR Luminosity, which is obtained from the UV luminosity using the definition of f_{obs}, on the x-axis. The calculated L_{IR} is expressed in units of $L_\odot$. The y-axis shows the number density of galaxies. The red curve represents the number density of IR galaxies at $z = 7$. The blue dotted line is derived from simulations conducted by Dayal et al. 2022. The yellow curve corresponds to the best-fit Schechter function that models the observed data points obtained from REBELS (yellow points).

The relationship between UV and IR luminosity is expressed through the dust attenuation parameter, $f_{\rm obs} = 1 - \mathrm{e}^{-\tau_{\rm eff}}$, which is the ratio of the dust-obscured to the intrinsic UV luminosity. The IR luminosity is then calculated using the following relation:

$$L_{\rm IR} = f_{\rm obs}\, L_{\rm UV} = (1 - e^{-\tau_{\rm eff}}) L_{\rm UV}$$

We move from the UV Luminosity function to the IR Luminosity function by following the chain rule again:

$$\begin{aligned}
\phi(L_{\rm IR}) &= \frac{dn}{dM_h}\frac{dM_h}{dL_{\rm IR}} \\
&= \frac{dn}{dM_h}\frac{dM_h}{dM_{\rm UV}}\frac{dM_{\rm UV}}{dL_{\rm IR}} \\
&= \phi(M_{\rm UV})\frac{dM_{\rm UV}}{dL_{\rm IR}}
\end{aligned}$$

$$\boxed{\phi(L_{\rm IR}) = \phi(M_{\rm UV})\tfrac{dM_{\rm UV}}{dL_{\rm IR}}}$$

Chapter 5

Conclusion and Future Developments

Using an analytical model, we derived the UV and IR Luminosity functions in the preceding chapter. To validate the model, we compared it with comprehensive observations from Bouwens (2022)[25], Naidu (2022)[13], and Finkelstein (2022)[14] based on data from JWST and ALMA. The model also predicted the amount of dust attenuation, which is proportional to the Star Formation Rate up to redshift $z \leq 9$. Interestingly, based on the latest data from JWST, the model predicts minimal dust attenuation for redshifts $z \geq 10$.

Further, the model is tested on various redshifts such as $z = 4, 6, 7$ and compared to available results. It has been observed that this model is in accordance with the data. Motivated by the success of UV LF, the model is extrapolated to calculate IR LF and compared to results available from Gruppioni 2020[22], Baruffet 2023[34], etc.

5.1 UV LF interpretation

According to the model, the minimum UV magnitude is $M_{\rm UV} = -22.3$ at $z = 7$. This $M_{\rm UV}$ corresponds to SFR $\simeq 130\,{\rm M}_\odot\,{\rm yr}^{-1}$. Due to the definition of $\tau_{\rm eff}$, galaxies with higher SFR are more attenuated, which results in smaller $M_{\rm UV}$. The lower branch of bi-valued UV LF does not affect the number density of the galaxies as the contribution is negligible. Hence, the model predicts that galaxies brighter than -22.3 at $z = 7$ are powered by an AGN. This prediction has also been found to be consistent with GOLDRUSH (Great Optically

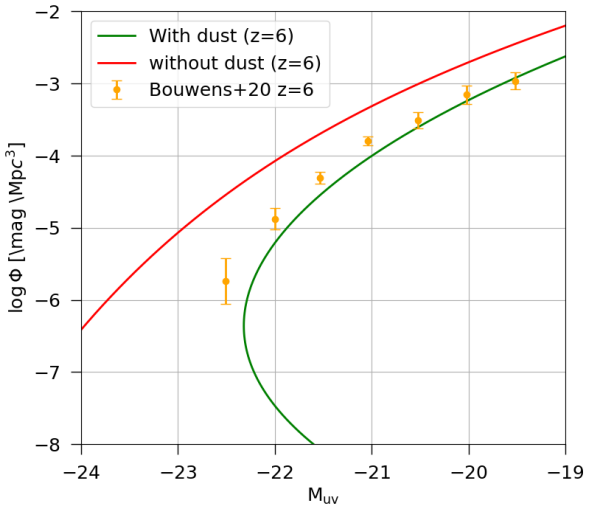

(a) $z = 6$

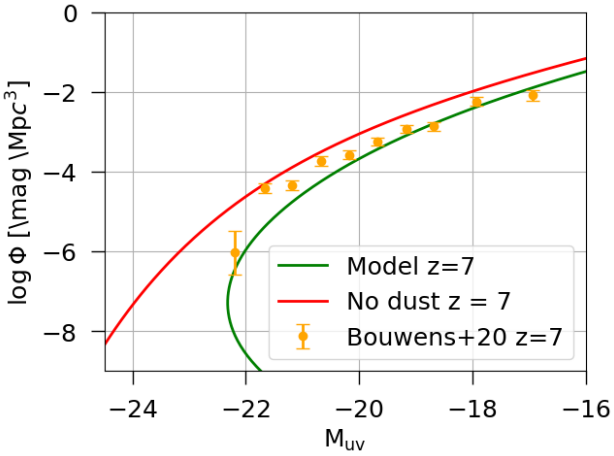

(b) $z = 7$

Figure 5.1: In this plot, the UV LF is compared with the data given by Bouwens et al. 2021 [25]

Luminous Dropout Research Using Subaru HSC) results. This program provides precise determinations of the very bright end of the galaxy UV LFs at $z = 4 - 7$. This program also investigates the astrophysical processes like AGN affecting the bright end of the Luminosity Function [35].

The model also predicts the abundance of highly obscured galaxies. For example, REBELS-25 - the brightest ($M_{\rm UV} = -21.7$) and most heavily obscured REBELS galaxy. This magnitude corresponds to SFR = 43 and 267 $\rm M_\odot\ yr^{-1}$. Since this galaxy is highly obscured, the

SFR is primarily driven by its large IR Luminosity, $\log(L_{\rm IR}/L_{\odot}) = 12.45^{+0.43}_{-0.45}$ with estimated SFR of $200^{+101}_{-64}\,{\rm M}_{\odot}\,{\rm yr}^{-1}$. This corresponds to the $\log(\phi) = -7.7$, and the difference concerning the no dust curve represents about ≈ 3 magnitudes of attenuation. SFR contribution evaluation of obscured and unobscured systems concludes that galaxies like REBELS-25 only contribute $\leq 1\%$ of the cosmic SFRD.

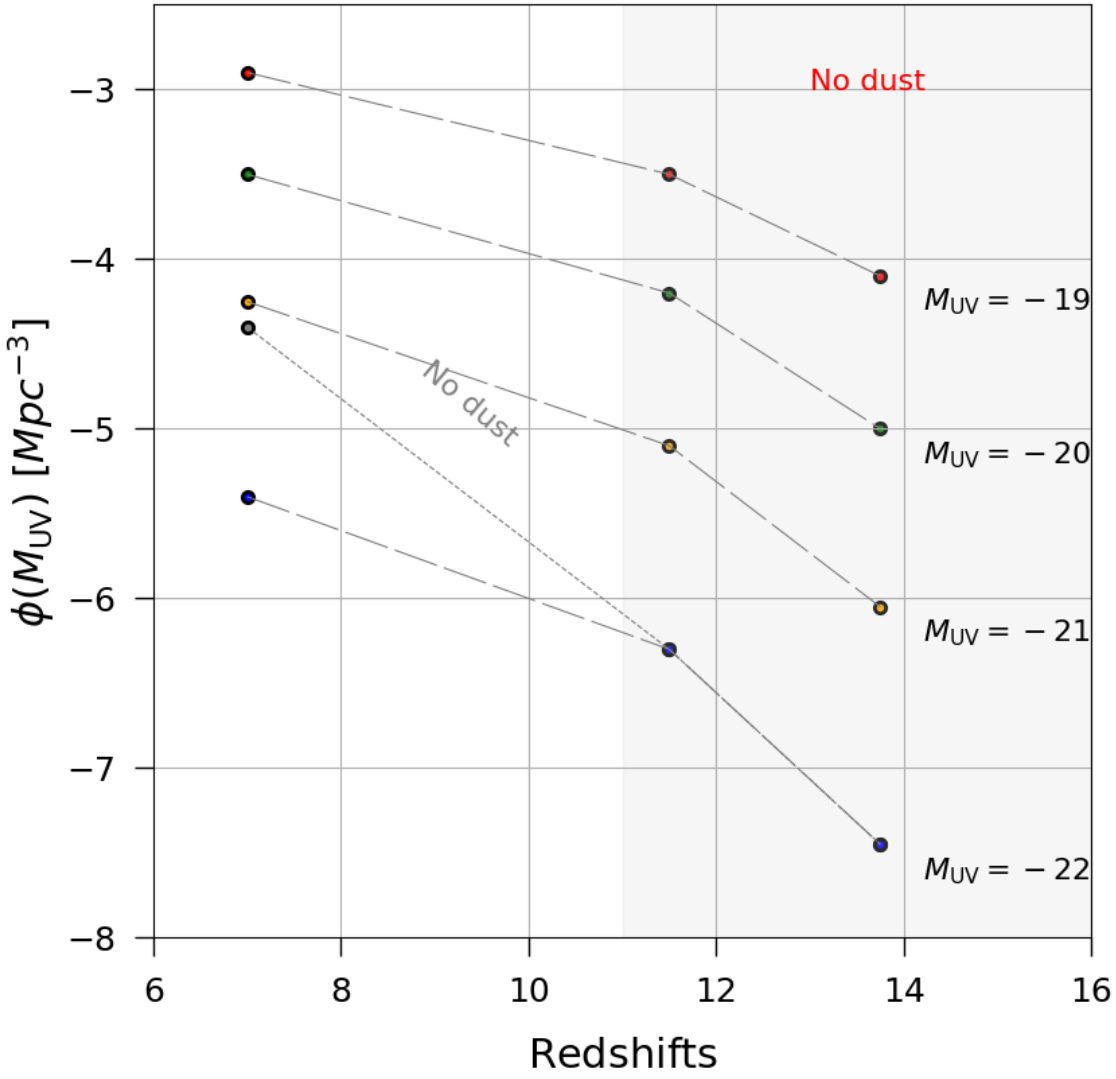

Figure 5.2: This plot depicts the luminosity density evolution according to the model for three different relevant redshifts 7, 11.5, 13.75. Each plot refers to different $M_{\rm UV}$. The grey point marked as no dust assumes $\tau_{\rm eff} = 0$. The model predicts minimal dust obscuration beyond $z \approx 11$. Hence all the points do not include dust attenuation.

Now, we use the model to interpret recent LF measurements at $z = 11.5$. The lack of evolution in the bright end of the UV-LF (Fig 5.2) is due to decreasing attenuation and

hence larger transmission of UV photons, which compensates for the decreasing host halo abundance towards higher redshifts. The model hypothesizes zero obscuration at $z = 11.5$ galaxies.

When $\tau_{\text{eff}} = 0$, the estimated number density matches the number density of GLz11/GLz13. This solution also satisfies the data point for GN-z11 (Oesch et al. 2016 [36]), which is a spectroscopically confirmed galaxy at z = 11 (Fig 5.3). As a further test, the LF is computed at $z = 13.75$ to compare it with another set of JWST detections by Donnan et al. 2022[12]. These detections show a single point of the LF in the highest redshift bin, $12.5 < z < 15$ (mean 13.75), containing five sources from JWST ERO and ERS NIR-Cam along with the COSMOS field. The number density for $\mathrm{M_{UV}} = -19.1$ correspond to $\log(\phi) = -4.77^{+0.24}_{-0.53}$. Assuming $\tau_{\text{eff}} = 0$, predicts $\log(\phi) = -4.1$, which is within 1σ from the observed value.

These findings conclude that recently discovered super early massive galaxies are virtually unaffected by dust attenuation. One of the possibilities is that due to a particular relative distribution of stars and dust, 1500Å radiation can leak out. Alternatively, the dust-to-stellar mass ratio is low for such galaxies. One of the other reasons can be the possibility of evacuation of dust as soon as the stars produce it due to radiation pressure. However, these systems would be poor FIR continuum emitters in all these cases.

5.2 IR LF interpretation

Using the model for the UV Luminosity function, we plot the IR Luminosity function by a variable transformation, where $L_{\text{IR}} = f_{\text{obs}} L_{\text{UV}} = (1 - e^{\tau_{\text{eff}}}) L_{\text{UV}}$. While the UV Luminosity function agrees with the observed data, we find tension in the data and theoretical IR Luminosity function.

Due to the lack of IR-based galaxy surveys, the observed data used in this thesis are from "UV-selected galaxies." ALMA scans the sky looking for the brightest galaxies in UV radiation $M_{\text{UV}} > -21$. We convert this data to L_{IR}. Hence, these surveys might be missing galaxies that are not detectable in UV due to various reasons (like entirely obscured by dust). We call such galaxies **UV dark galaxies**. These galaxies can be detected in IR surveys.

We would proceed to calculate the number density of these missing galaxies. Let us call

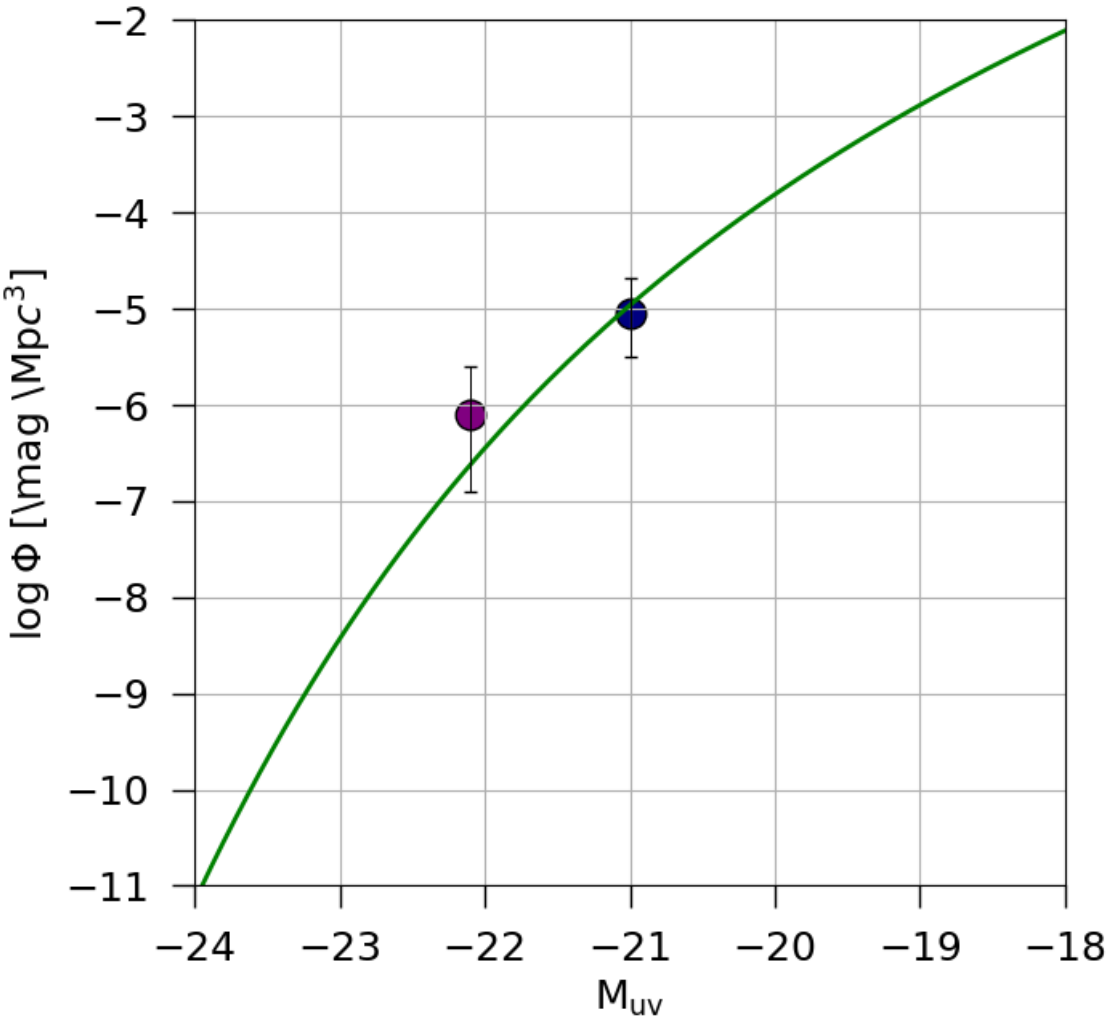

Figure 5.3: The blue point refers to the Naidu et al 2022 [13] combined GL-z11/GL-z13 galaxies while the brown point is the GN-z11 [36] at $z = 11.1$. The green line predicts the UV LF according to the model assuming negligible dust obscuration. The model is in accordance with both the observations.

the Luminosity function fitting the observation (which is essentially the Schechter Function) as ϕ_{SF}. We can define the number density of missing galaxies, ϕ_*:

$$\phi_*(z) = \phi_{\mathrm{SF}}(z) - \phi_{\mathrm{IR}}(z)$$

ϕ_{IR} is the IR luminosity function calculated using the proposed model. ϕ_* is plotted at various redshifts ($z = 4, 6, 7$ to maintain continuity). We can also calculate the percentage

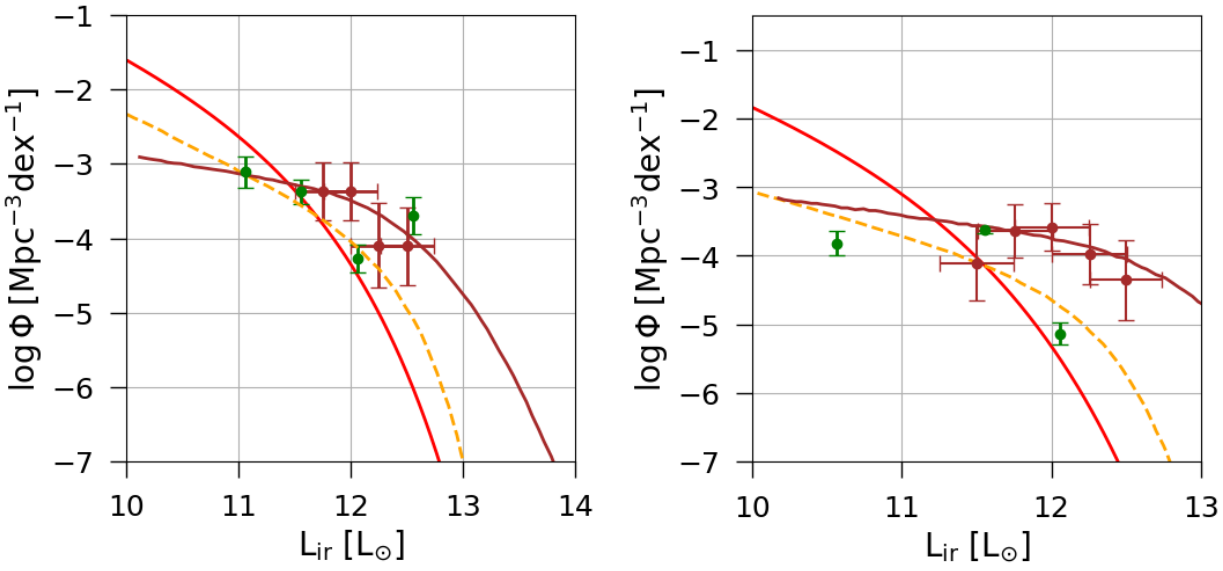

(a) $z = 4$ (b) $z = 5.5$

Figure 5.4: Alongwith Fig 4.3, we also plot at redshift 4 and 5.5. The model (red plot) is then compared with IllustrisTNG simulation (yellow dotted line) and observations from Gruppioni et al. 2020 [22] (brown filled points). The brown line refers to the best fir Schechter function for these points. We have also included Yan et al. 2020 [37] data points (green) for comparison. Since these observations are dependent on UV-selected samples, these observations do not account for UV faint and UV dark galaxies, which could significantly affect the shape of IR Luminosity Function.

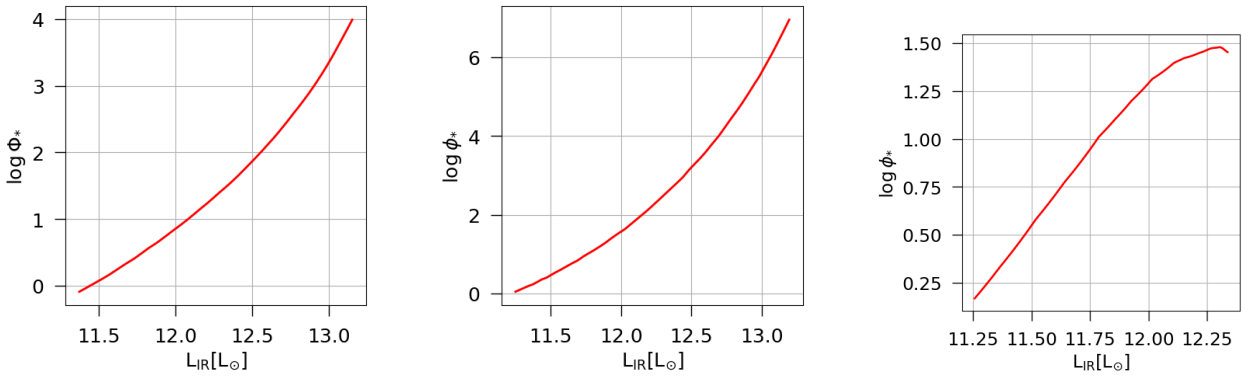

(a) $z = 4$ (b) $z = 5.5$ (c) $z = 7$

Figure 5.5: In the first two plots, the Schechter function is based on the best-fit points of ALPINE galaxies which detects galaxies till $z < 6$.

of these missing galaxies:

$$\phi_*(z)\% = \frac{\phi_*(z)}{\phi_{\text{IR}}(z)} \times 100$$

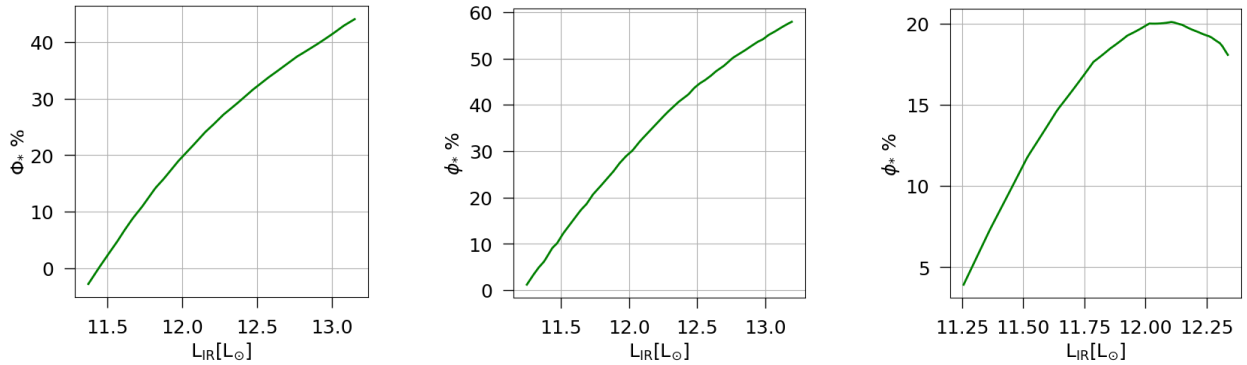

(a) $z = 4$ (b) $z = 5.5$ (c) $z = 7$

Figure 5.6: Percentage of missing galaxies at three different redshift

From Fig no. 5.5 and 5.6, we can infer that more highly luminous galaxies are missing in lower redshifts than in higher redshifts. The percentage values of these missing galaxies can reach as high as 60% at redshift $z = 5.5$. More highly IR luminous galaxies are missing. Moving from $z = 4$ to $z = 5.5$, we see an upward trend in missing galaxies, and then the percentage reduces at $z = 7$. However, the comparison might not be accurate as the Schechter function derived in the first two redshifts uses ALPINE data, and the third one is the REBELS data. Due to the detection methods, the errors given by both programs are very different. ALPINE is known to provide data with significant errors.

The goal of moving forward would be to determine the possible reasons behind these non-detections. With the advancement of technology and more upcoming observatories and telescopes like ATLAST and ORIGINS aimed at broad sky areas detecting blind, sub-mm wavelengths, the detection of these SMGs and UV Dark Galaxies would be feasible, and it would allow us to constrain the IR Luminosity Function to precision.

5.3 Summary

The thesis proposes a minimal galaxy evolution model that considers the halo mass function (HMF), supernova feedback, and dust attenuation calibrated based on the ALMA REBELS data. The model accurately predicts the Luminosity Function at $z = 7$ compared to various

observations and other redshifts $z = 6$. The model predicts that the effective optical depth, τ_{eff}, is proportional to the star formation rate (SFR) to the power of 1.45. This implies that galaxies brighter than $M_{\text{UV}} = -22.3$ at $z = 7$ are dust-obscured, resulting in a lower observed magnitude and a significant active galactic nucleus (AGN) contribution.

The model also predicts the contribution of heavily obscured luminous infrared galaxies such as REBELS-25 to be less than or equal to 1% of the cosmic star formation rate density (SFRD). Moreover, the model successfully predicts the abundance of super-early, bright James Webb Space Telescope (JWST) candidates at $z = 11.5$ and $z = 13.5$ by assuming minimal dust attenuation at high redshifts. This assumption is supported by the very blue ultraviolet slopes of the highest redshift candidates, suggesting efficient dust ejection during the early phases of galaxy evolution.

The weak evolution of the bright end of the luminosity function from $z = 7 - 14$ can be attributed to decreasing dust attenuation, resulting in more luminous galaxies compensating for the increasing rarity of host halos.

Further calculations have been carried out for the infrared (IR) luminosity function (LF). However, the model shows discrepancies with the scattered observations at different redshifts. The model under-predicts the IR luminosity function compared to the Schechter fit. This could be attributed to the presence of "UV dark" galaxies, which are completely obscured by dust and go unnoticed in UV-selected galaxy samples used for the observations. As a result, such galaxies with high IR luminosity are not accounted for in the current observations.

The model estimates these missing galaxies' number, density, and percentage to address this. Future observational missions like ORIGINS, which will study star formation using IR radiation and other spectroscopic capabilities (proposed 2035), and ATLAST, which is ALMA 2.0, would operate at sub-millimeter and millimeter wavelengths, are expected to detect such galaxies and provide a better constraint for the IR LF with higher precision. More extensive studies can be done by calculating the SFRD at both UV and IR and by looking at the trend of missing galaxies across redshift to figure out the phenomena behind this.

5.4 Original Work

This section outlines the original work conducted in this thesis, which includes:

1. A recalculation and correction of the model proposed by Ferrara et al. 2022 [27] from scratch.
2. Data analysis of ALMA REBELS data to establish the relationships between M_{UV} and τ_{eff}.
3. Creation of a novel analytical model for the IR LF, which is a corrected version and one of the first of its kind.
4. Identification of a discrepancy between the novel IR LF model and the existing observational model, with the suggestion that missing galaxies known as "UV dark galaxies" may be a possible cause.
5. Development of a simple model for UV dark galaxies, which can be tested using future data from ORIGINS and ATLAST.
6. Analysis and interpretation of the model in both UV and IR.

Appendix A

Random Walk Method

In Section 1.3, we discussed the large-scale structure formation and the derivation of the Halo Mass Function. This chapter is written with the help of notes of Prof Tirthankar Roy Choudhury on Halo Mass Function at NCRA. We used the random walk method to solve the "cloud in cloud" problem. As mentioned in the section, for every random walk trajectory which goes above the δ_c barrier at M_1, there is an equal probability that it will continue going above or below δ_c for $M < M_1$. Hence,

$$\begin{aligned} f_{\rm coll}(> M_h, z) &= \int_{\delta_c}^{\infty} P(\delta_M, R, z) d\delta_M + \int_{-\infty}^{\delta_c} C(\delta_M, R, z) d\delta_M \\ &= 2 \times \int_{\delta_c}^{\infty} P(\delta_M, R, z) d\delta_M \end{aligned}$$

In this section, we will resolve the problem by going into detail about how the random walk method can be implemented to the problem.

A.1 Formation of Halos

We will restart by explaining the formation of halos in more straightforward terms to get a flavour. The formation of collapsed objects is crucial for forming galaxies. We need to find the HMF for a cosmic density field. This cannot be done analytically as the entire problem

is non-linear. We would explain the theoretical model to capture the basics of its formation. According to the spherical approximation, a region collapses and forms a virialized object when the linear density contrast within the region exceeds $\delta_c \approx 1.686$.

Let us suppose the initial density field $\delta(z, \mathbf{x})$. According to linear theory, it grows as $D(z)$ in the linear theory.

$$\delta(z, \mathbf{x}) = D(z)\delta(\mathbf{x})$$

where $\delta(\mathbf{x})$ is the linearly extrapolated field at $z = 0$. Hence a region of comoving radius X collapses when:

$$\delta_X(z, \mathbf{x}) \geq \delta_c \implies \delta_X(\mathbf{x}) \geq \frac{\delta_c}{D(z)} \equiv \delta_c(z)$$

A.2 Random Walk

Now we can obtain the HMF analytically by using *Excursion set formalism*. We concentrate on a given point $\mathbf{x}$ in the linear density field. We smooth the field using a spherical window of radius X. Assume a large radius such as $X \to \infty$, and then compute $\delta_X\mathbf{x}$. For a large enough X, $\delta_X \to 0$. Then we take a smaller radius and compute $\delta_X(\mathbf{x})$. We continue with this process as X is reducing to a smaller number. We observe that the smoothed quantity δ_X now is carrying out a "random walk" as a function of smoothing radius X. Hence, with some modifications, we can map this problem to a random walk.

Let us assume the variable corresponding to the random walk steps as $s \equiv \sigma^2(X) = \sigma^2(M)$ where $M = 4\pi X^3\bar{\rho}_0/3$ instead of X. We can now say that s is a monotonically decreasing function of X and M. Also, as $X \to \infty$, $s \to 0$. Hence, all trajectories start from the origin in $\delta_X - s$ space. Each location $\mathbf{x}$ corresponds to a trajectory $\delta_X(s)$ reflecting the value of the density field at that location which has been smoothed with a filter of radius $X(s)$

Before going further, let us recap some basics of random walks. Let $\mathbf{x_1}, ..., \mathbf{x_N}$ are

random variables which can take values ± 1 with equal probabilities i.e $1/2$:

$$\mathcal{P}(\mathbf{x_i} = 1) = \mathcal{P}(\mathbf{x_i} = -1) = \frac{1}{2}$$

Here, we can think of x_i as the distance traveled in a step by a random walker. Let $\mathcal{D}_N = \sum_i^N \mathbf{x}_i$ be the distance after N steps, which is also a random variable. So its expectation value is:

$$\langle \mathcal{D}_N \rangle = \sum_{i=1}^{N} \langle \mathbf{x}_i \rangle = \sum_{i}^{N} \left[\mathcal{P}(\mathbf{x}_i = 1) \times (+1) + \mathcal{P}(\mathbf{x}_i = -1) \times (-1) \right] = 0$$

Due to symmetry in probability, the average distance traveled by an ensemble of walkers would be zero. Similarly, the variance in the number of steps is given by:

$$\begin{aligned} \langle \mathcal{D}_N^2 \rangle &= \sum_{i,j=1}^{N} \langle \mathbf{x}_i \mathbf{x}_j \rangle \\ &= \begin{cases} 0 \text{ if } i \neq j & \text{(uncorrelated steps)} \\ \sum_{i=1}^{N} \langle \mathbf{x}_i^2 \rangle = N \text{ otherwise} \end{cases} \end{aligned}$$

The density field smoothed over some length X can be written as:

$$\delta_X(\mathbf{x}) = \int d^3y \delta(\mathbf{y}) W_X(|\mathbf{y} - \mathbf{x}|)$$

In Fourier space, the above equation can be written as follows:

$$\delta_X(\mathbf{x}) = \int \frac{d^3k}{(2\pi)^3} \mathrm{e}^{i\mathbf{k}.\mathbf{x}} \delta(\mathbf{k}) W_X^*(k)$$

We can write the correlation across different filter scales as follows:

$$\begin{aligned} \langle \delta_{X_1}(\mathbf{x}) \delta_{X_2}(\mathbf{x}) \rangle &= \int \frac{d^3k}{(2\pi)^3} \frac{d^3k'}{(2\pi)^3} e^{i\mathbf{k}.\mathbf{x}} e^{i\mathbf{k}'.\mathbf{x}} \langle \delta(\mathbf{k}) \delta^*(\mathbf{k}') \rangle W_{X_1}^*(k) W_{X_2}(k') \\ &= \int_0^\infty \frac{dk}{k} \Delta^2(k) W_{X_1}^*(k) W_{X_2}(k) \end{aligned}$$

Under a certain special case, the above equation takes the following form:

$$\langle \delta_X^2(\mathbf{x}) \rangle = \int_0^\infty \frac{dk}{k} \Delta^2(k) W_X^*(k) W_X(k) \equiv \sigma^2(X) \equiv s(X)$$

Having done this, we can find the correspondence of our problem with the random walk problem:

$$\begin{aligned} x_i &\iff \delta \, , \mathcal{D}_N \iff \delta_X \\ \langle \mathcal{D}_N \rangle = 0 &\iff \langle \delta_X \rangle = 0 \\ \langle \mathcal{D}_N^2 \rangle = N &\iff \langle \delta_X^2 \rangle = s \end{aligned}$$

Since X, M, s all are used for measuring the smoothing scale; we can use the notation $\delta_X \equiv \delta_s$. We can show that the different steps are uncorrelated for the random walk correspondence to work by using the shark-k filter:

$$W_X(k) = \theta \left(\frac{1}{X} - k \right)$$

$$W_X(r) = \frac{\sin(r/X) - (r/X)\cos(r/X)}{2\pi^2 r^3}$$

As we know, the condition for collapse at redshift z is:

$$\delta_X(z, \mathbf{x}) \geq \delta_c \implies \delta_X(\mathbf{x}) \geq \frac{\delta_c}{D(z)} \equiv \delta_c(z)$$

We can interpret $\delta_c(z)$ as a "barrier" that the random walker should cross for forming halos. The condition for halo formation will be given by random walks crossing the barrier the first time. If the random walker crosses any other time, it will correspond to larger s hence smaller length scales which would form structures within the large halo. As we can see, δ_c increases at higher/early redshift, which means it is a higher barrier; hence the random walkers have to travel more at high redshift. It implies halos that collapsed at early times will have larger values of s and hence smaller values of M. Hence we can summarise small mass haloes form first. This is called "hierarchical structure formation."

Now we would use this formalism to calculate the halo mass function. We would start by assuming that the random walk crosses the barrier at s_0 for the first time. Then expectedly, it would form a collapsed object of mass corresponding to s_0 at a redshift corresponding to $D(z) = \delta_c/\delta_0$. We would denote the fraction of random walks crossing the barrier at a point between $(s, s+ds)$ as $f(\delta, s)ds$. At $\delta + \delta_c(z)$, this probability would be the same as a fraction of points $f(M, z)dM$, which collapses to objects of mass range M and $M + dM$ at redshift z. Each of these points has a comoving volume of $M/\bar{\rho}_0$. Hence,

$$f(\delta_c(z), s)ds = \frac{M}{\bar{\rho}_0} n(M, z)dM$$

$$n(M, z) = \frac{\bar{\rho}_0}{M} f(\delta_c(z), s) \left| \frac{ds}{dM} \right|$$

This equation gives the number of halos per unit comoving volume per unit mass range, also known as the "halo mass function." For calculating $f(\delta, s)$, we will consider the fraction of trajectories $P(\delta_0, s_0)d\delta_0$ which at $s = s_0$ has values between $(\delta_0, delta_0 + d\delta_0)$. The Gaussianity of the linear density field implies:

$$\mathcal{P}\left(\delta_0, s_0\right) = \frac{1}{\sqrt{2\pi s_0}} \mathrm{e}^{-\delta_0^2/2s_0}.$$

At some point $s = s_1 < s_0$ the trajectories must have first crossed the point $\delta = \delta_1 < \delta_0$. Out of $f(\delta_1, s_1)ds_1$ fraction of points, let $\mathcal{P}\left(\delta_0, s_0 \mid \delta_1, s_1, \mathrm{FC}\right) \mathrm{d}\delta_0$ have value between $(\delta_0, \delta_0 + \mathrm{d}\delta_0)$ at s_0. Hence the fraction of points that first crosses δ_1 between $(s_1, s_1 + ds_1)$ and have value between $\delta_0, \delta_0 + d\delta_0$ at s_0 is:

$$f(\delta_1, s_1)ds_1 \times P(\delta_0, s_0 \mid \delta_1, s_1, \mathrm{FC})d\delta_0$$

We can integrate the above quantity over s_1 to get the fraction of points irrespective of where they first crossed δ_1:

$$P\left(\delta_0, s_0\right) d\delta_0 = \int_0^{s_0} ds_1 f\left(\delta_1, s_1\right) P\left(\delta_0, s_0 \mid \delta_1, s_1, \mathrm{FC}\right) d\delta_0$$

Since the subsequent steps are uncorrelated with the previous ones, we can assume that after

the trajectory crosses δ_1 at s_1, a new random walk begins at (δ_1, s_1)

$$\begin{aligned} P\left(\delta_0, s_0 \mid \delta_1, s_1, \mathrm{FC}\right) d\delta_0 &= P\left(\delta_0 - \delta_1, s_0 - s_1\right) d\delta_0 \\ &= \frac{1}{\sqrt{s_0 - s_1}\sqrt{2\pi}} \mathrm{e}^{-(\delta_0-\delta_1)^2/2(s_0-s_1)}. \end{aligned}$$

Using these quantities, we want to determine $f(\delta_1, s_1)$. We can do so by integrating $P(\delta_0, s_0)$ over δ_0:

$$\begin{aligned} \int_{\delta_1}^{\infty} d\delta_0 P\left(\delta_0, s_0\right) &= \int_0^{s_0} ds_1 f\left(\delta_1, s_1\right) \int_{\delta_1}^{\infty} d\delta_0 P\left(\delta_0, s_0 \mid \delta_1, s_1, \mathrm{FC}\right), \\ \frac{1}{\sqrt{2\pi s_0}} \int_{\delta_1}^{\infty} d\delta_0 \mathrm{e}^{-\delta_0^2/2s_0} &= \frac{1}{\sqrt{s_0 - s_1}\sqrt{2\pi}} \int_0^{s_0} ds_1 f\left(\delta_1, s_1\right) \int_{\delta_1}^{\infty} d\delta_0 \mathrm{e}^{-(\delta_0-\delta_1)^2/2(s_0-s_1)}, \\ \frac{1}{2} \operatorname{erfc}\left(\frac{\delta_1}{\sqrt{2s_0}}\right) &= \frac{1}{\sqrt{s_0 - s_1}\sqrt{2\pi}} \int_0^{s_0} ds_1 f\left(\delta_1, s_1\right) \int_0^{\infty} \mathrm{d}\bar{\delta}_0 \mathrm{e}^{-\bar{\delta}_0^2/2(s_0-s_1)} \\ &= \int_0^{s_0} ds_1 f\left(\delta_1, s_1\right) \times \frac{1}{2} \end{aligned}$$

So,

$$\int_0^{s_0} ds_1 f\left(\delta_1, s_1\right) = \operatorname{erfc}\left(\frac{\delta_1}{\sqrt{2s_0}}\right)$$

We can differentiate the above equation to show that:

$$f\left(\delta_1, s_0\right) = \frac{\delta_1}{\sqrt{2\pi s_0^3}} \mathrm{e}^{-\delta_1^2/2s_0}$$

Plugging this into the halo mass function, we derive the Press Schechter mass function:

$$\begin{aligned} n(M, z) &= \frac{\bar{\rho}_0}{M} f\left(\delta_c(z), s\right) \left|\frac{\mathrm{d}s}{\mathrm{d}M}\right| \\ &= \frac{\bar{\rho}_0}{M} \left|\frac{\mathrm{d}s}{\mathrm{d}M}\right| \times \frac{\delta_c(z)}{\sqrt{2\pi s^3}} \mathrm{e}^{-\delta_c^2(z)/2s} \\ &= \frac{1}{\sqrt{2\pi}} \frac{\bar{\rho}_0}{M} \frac{\delta_c(z)}{s^{3/2}} \left|\frac{\mathrm{d}s}{\mathrm{d}M}\right| \mathrm{e}^{-\delta_c^2(z)/2s}. \end{aligned}$$

Appendix B

Star Forming Efficiency

Star Forming Efficiency is the fraction of the interstellar gas which forms a star over the total amount of the gas present. Our model uses the star-forming efficiency proposed by Dayal et al. 2014. The derivation entails simple physics of galaxy formation. In this section, we will be showing the same.

A straightforward model for galaxy formation can be built solely on a balance between the amount of Type II Supernovae (SNII) energy available to drive winds and the gravitational potential of the host DM halo. The primary idea behind this is: Star formation in a galaxy would be quenched if the SNII Kinetic energy is larger than the binding energy of a halo. However, the halos having B.E greater than SNII K.E will lose part of their gas and continue forming stars. The mathematical formulation involves introducing feedback-limited star formation efficiency.

Radiative cooling is an efficient process in dense low-mass halos at high redshift. If it continues, it leads to an overproduction of stars and too many baryons locked up in condensed halos, termed "overcooling." This problem is removed by introducing SN feedback. SN Feedback decreases the SFE of small halos by ejecting their gas and quenching star formation.

$M_*(z)$ amount of star formation imparts the ISM with the following amount of SNII energy,

$$E_{\rm SN} = f_w E_{51} \nu M_*(z) \equiv f_w v_s^2 M_*(z)$$

Each SNII imparts instantaneous explosion energy of $E_{51} = 10^{51}$ erg to the ISM, and $\nu = [134\ M_\odot]^{-1}$ is the number of SNII per stellar mass formed for a Salpeter IMF between $0.1 - 100 M_\odot$. Hence $v_s = 611 \mathrm{km\,s^{-1}}$. f_w is the ratio of explosion energy converted to the kinetic form to drive the wind. Now talking about the B.E Part, we introduce E_{ej}, which is the energy required to unbind and eject all the ISM gas:

$$E_{ej} = \frac{1}{2}\left[M_{g,i}(z) - M_*(z)\right] v_e^2$$

$M_{g,i}(z)$ is the mass of gas present in the galaxy at any epoch z. While the terms within the brackets imply the removal of gas by SN ejections which does not get converted to stars. Further, the relation between escape velocity and rotational velocity is $v_e = \sqrt{2} v_c$. Now the ejection efficiency, f_*^{ej} is the fraction of has that must be converted into stars to blow away the remaining gas from the galaxy and is calculated by an equation with previous two energies ($E_{ej} \leq E_{SN}$). Hence,

$$f_*^{ej}(z) = \frac{v_c^2(z)}{v_c^2(z) + f_w v_s^2}$$

The effective efficiency represents the maximum fraction of gas that can be converted into stars in a galaxy without expelling all the remaining gas; in other words, star formation efficiency:

$$f_*^{\mathrm{eff}} = \min[f_*, f_*^{ej}]$$

As v_c scales with the halo mass M_h, efficient star formers, which are hosted by large DM halos, can convert with f_* star formation efficiency while feedback limited systems can form stars with maximum efficiency by f_{ej} that decreases with decreasing halo mass. To match the bright and faint ends of the evolving UV LF, we require $f_* = 0.03$ and $f_w = 0.1$.

Bibliography

[1] R A A Bowler, M J Jarvis, J S Dunlop, R J McLure, D J McLeod, N J Adams, B Milvang-Jensen, and H J McCracken. A lack of evolution in the very bright end of the galaxy luminosity function from z 8 to 10. *Monthly Notices of the Royal Astronomical Society*, 493(2):2059–2084, 02 2020.

[2] Yuichi Harikane, Yoshiaki Ono, Masami Ouchi, Chengze Liu, Marcin Sawicki, Takatoshi Shibuya, Peter S. Behroozi, Wanqiu He, Kazuhiro Shimasaku, Stephane Arnouts, Jean Coupon, Seiji Fujimoto, Stephen Gwyn, Jiasheng Huang, Akio K. Inoue, Nobunari Kashikawa, Yutaka Komiyama, Yoshiki Matsuoka, and Chris J. Willott. Goldrush. iv. luminosity functions and clustering revealed with 4,000,000 galaxies at z 2–7: Galaxy–agn transition, star formation efficiency, and implication for evolution at z gt; 10. *The Astrophysical Journal Supplement Series*, 259(1):20, mar 2022.

[3] Jaan Einasto. Dark matter, 2010.

[4] et al. iplanck/i2018 results. *Astronomy &amp Astrophysics*, 641:A6, sep 2020.

[5] A. R. Liddle and D. H. Lyth. Trends in large-scale structure observations and the likelihood of early reionization. *Monthly Notices of the Royal Astronomical Society*, 273(4):1177–1184, apr 1995.

[6] William H. Press and Paul Schechter. Formation of galaxies and clusters of galaxies by self-similar gravitational condensation. *apj*, 187:425–438, feb 1974.

[7] Ravi K. Sheth and Giuseppe Tormen. Large-scale bias and the peak background split. *Monthly Notices of the Royal Astronomical Society*, 308(1):119–126, sep 1999.

[8] Nicha Leethochawalit, Guido Roberts-Borsani, Takahiro Morishita, Michele Trenti, and Tommaso Treu. The uv luminosity functions of bright z¿8 galaxies: Determination from 0.41 deg2 of hst observations along sim 300 independent sightlines. 2022.

[9] P. A. Oesch, R. J. Bouwens, G. D. Illingworth, I. Labbé , and M. Stefanon. The dearth of iz/i $\sim$ 10 galaxies in all iHST/i legacy fields—the rapid evolution of the galaxy population in the first 500 myr. *The Astrophysical Journal*, 855(2):105, mar 2018.

[10] R. A. A. Bowler, J. S. Dunlop, R. J. McLure, H. J. McCracken, B. Milvang-Jensen, H. Furusawa, Y. Taniguchi, O. Le Fè vre, J. P. U. Fynbo, M. J. Jarvis, and B. Häußler. The galaxy luminosity function atiz/ib$\simeq$ 6/band evidence for rapid evolution in the bright end fromiz/ib$\simeq$ 7/btob5/b. *Monthly Notices of the Royal Astronomical Society*, 452(2):1817–1840, jul 2015.

[11] Khusanova, Y., Le Fèvre, O., Cassata, P., Cucciati, O., Lemaux, B. C., Tasca, L. A. M., Thomas, R., Garilli, B., Le Brun, V., Maccagni, D., Pentericci, L., Zamorani, G., Amorín, R., Bardelli, S., Castellano, M., Cassarà, L. P., Cimatti, A., Giavalisco, M., Hathi, N. P., Ilbert, O., Koekemoer, A. M., Marchi, F., Pforr, J., Ribeiro, B., Schaerer, D., Tresse, L., Vergani, D., and Zucca, E. Uv and lyinosity functions of galaxies and star formation rate density at the end of hi reionization from the vimos ultradeep survey (vuds). *A&A*, 634:A97, 2020.

[12] C T Donnan, D J McLeod, J S Dunlop, R J McLure, A C Carnall, R Begley, F Cullen, M L Hamadouche, R A A Bowler, D Magee, H J McCracken, B Milvang-Jensen, A Moneti, and T Targett. The evolution of the galaxy UV luminosity function at redshifts z $\simeq$ 8 – 15 from deep iJWST/i and ground-based near-infrared imaging. *Monthly Notices of the Royal Astronomical Society*, 518(4):6011–6040, nov 2022.

[13] Rohan P. Naidu, Pascal A. Oesch, Pieter van Dokkum, Erica J. Nelson, Katherine A. Suess, Gabriel Brammer, Katherine E. Whitaker, Garth Illingworth, Rychard Bouwens, Sandro Tacchella, Jorryt Matthee, Natalie Allen, Rachel Bezanson, Charlie Conroy, Ivo Labbe, Joel Leja, Ecaterina Leonova, Dan Magee, Sedona H. Price, David J. Setton, Victoria Strait, Mauro Stefanon, Sune Toft, John R. Weaver, and Andrea Weibel. Two remarkably luminous galaxy candidates at z $\approx$ 10–12 revealed by JWST. *The Astrophysical Journal Letters*, 940(1):L14, nov 2022.

[14] Steven L. Finkelstein, Micaela B. Bagley, Pablo Arrabal Haro, Mark Dickinson, Henry C. Ferguson, Jeyhan S. Kartaltepe, Casey Papovich, Denis Burgarella, Dale D. Kocevski, Marc Huertas-Company, Kartheik G. Iyer, Anton M. Koekemoer, Rebecca L. Larson, Pablo G. Pérez-González, Caitlin Rose, Sandro Tacchella, Stephen M. Wilkins, Katherine Chworowsky, Aubrey Medrano, Alexa M. Morales, Rachel S. Somerville, L. Y. Aaron Yung, Adriano Fontana, Mauro Giavalisco, Andrea Grazian, Norman A. Grogin, Lisa J. Kewley, Allison Kirkpatrick, Peter Kurczynski, Jennifer M. Lotz, Laura Pentericci, Nor Pirzkal, Swara Ravindranath, Russell E. Ryan, Jonathan R. Trump, Guang Yang, Omar Almaini, Ricardo O. Amorín, Marianna Annunziatella, Bren E. Backhaus, Guillermo Barro, Peter Behroozi, Eric F. Bell, Rachana Bhatawdekar, Laura Bisigello, Volker Bromm, Véronique Buat, Fernando Buitrago, Antonello Calabrò, Caitlin M. Casey, Marco Castellano, Óscar A. Chávez Ortiz, Laure Ciesla, Nikko J. Cleri, Seth H. Cohen, Justin W. Cole, Kevin C. Cooke, M. C. Cooper, Asantha R. Cooray, Luca Costantin, Isabella G. Cox, Darren Croton, Emanuele Daddi, Romeel Davé, Alexander de La Vega, Avishai Dekel, David Elbaz, Vicente Estrada-Carpenter,

Sandra M. Faber, Vital Fernández, Keely D. Finkelstein, Jonathan Freundlich, Seiji Fujimoto, Ángela García-Argumánez, Jonathan P. Gardner, Eric Gawiser, Carlos Gómez-Guijarro, Yuchen Guo, Kurt Hamblin, Timothy S. Hamilton, Nimish P. Hathi, Benne W. Holwerda, Michaela Hirschmann, Taylor A. Hutchison, Anne E. Jaskot, Saurabh W. Jha, Shardha Jogee, Stéphanie Juneau, Intae Jung, Susan A. Kassin, Aurélien Le Bail, Gene C. K. Leung, Ray A. Lucas, Benjamin Magnelli, Kameswara Bharadwaj Mantha, Jasleen Matharu, Elizabeth J. McGrath, Daniel H. McIntosh, Emiliano Merlin, Bahram Mobasher, Jeffrey A. Newman, David C. Nicholls, Viraj Pandya, Marc Rafelski, Kaila Ronayne, Paola Santini, Lise-Marie Seillé, Ekta A. Shah, Lu Shen, Raymond C. Simons, Gregory F. Snyder, Elizabeth R. Stanway, Amber N. Straughn, Harry I. Teplitz, Brittany N. Vanderhoof, Jesús Vega-Ferrero, Weichen Wang, Benjamin J. Weiner, Christopher N. A. Willmer, Stijn Wuyts, Jorge A. Zavala, and CEERS Team. A Long Time Ago in a Galaxy Far, Far Away: A Candidate z 12 Galaxy in Early JWST CEERS Imaging. , 940(2):L55, December 2022.

[15] Rowlands. Dust in galaxies throughout cosmic time. 2013.

[16] Rebecca A. Bernstein, Wendy L. Freedman, and Barry F. Madore. The First Detections of the Extragalactic Background Light at 3000, 5500, and 8000 Å. III. Cosmological Implications. , 571(1):107–128, May 2002.

[17] B. T. Draine and H. M. Lee. Optical Properties of Interstellar Graphite and Silicate Grains. , 285:89, October 1984.

[18] Joseph C. Weingartner and B. T. Draine. Dust Grain-Size Distributions and Extinction in the Milky Way, Large Magellanic Cloud, and Small Magellanic Cloud. , 548(1):296–309, February 2001.

[19] Viktor Zubko, Eli Dwek, and Richard G. Arendt. Interstellar Dust Models Consistent with Extinction, Emission, and Abundance Constraints. , 152(2):211–249, June 2004.

[20] Aigen Li and B. T. Draine. Infrared Emission from Interstellar Dust. II. The Diffuse Interstellar Medium. , 554(2):778–802, June 2001.

[21] B. T. Draine. Interstellar Dust Grains. , 41:241–289, January 2003.

[22] C. Gruppioni, M. Bé thermin, F. Loiacono, O. Le Fèvre, P. Capak, P. Cassata, A. L. Faisst, D. Schaerer, J. Silverman, L. Yan, S. Bardelli, M. Boquien, R. Carraro, A. Cimatti, M. Dessauges-Zavadsky, M. Ginolfi, S. Fujimoto, N. P. Hathi, G. C. Jones, Y. Khusanova, A. M. Koekemoer, G. Lagache, B. C. Lemaux, P. A. Oesch, F. Pozzi, D. A. Riechers, G. Rodighiero, M. Romano, M. Talia, L. Vallini, D. Vergani, G. Zamorani, and E. Zucca. The ALPINE-ALMA [CII] survey. *Astronomy &amp Astrophysics*, 643:A8, oct 2020.

[23] J. A. Zavala, C. M. Casey, S. M. Manning, M. Aravena, M. Bethermin, K. I. Caputi, D. L. Clements, E. da Cunha, P. Drew, S. L. Finkelstein, S. Fujimoto, C. Hayward,

J. Hodge, J. S. Kartaltepe, K. Knudsen, A. M. Koekemoer, A. S. Long, G. E. Magdis, A. W. S. Man, G. Popping, D. Sanders, N. Scoville, K. Sheth, J. Staguhn, S. Toft, E. Treister, J. D. Vieira, and M. S. Yun. The Evolution of the IR Luminosity Function and Dust-obscured Star Formation over the Past 13 Billion Years. , 909(2):165, March 2021.

[24] Xuejian Shen, Mark Vogelsberger, Dylan Nelson, Sandro Tacchella, Lars Hernquist, Volker Springel, Federico Marinacci, and Paul Torrey. High-redshift predictions from IllustrisTNG – III. infrared luminosity functions, obscured star formation, and dust temperature of high-redshift galaxies. *Monthly Notices of the Royal Astronomical Society*, 510(4):5560–5578, jan 2022.

[25] R. J. Bouwens, R. Smit, S. Schouws, M. Stefanon, R. Bowler, R. Endsley, V. Gonzalez, H. Inami, D. Stark, P. Oesch, J. Hodge, M. Aravena, E. da Cunha, P. Dayal, I. de Looze, A. Ferrara, Y. Fudamoto, L. Graziani, C. Li, T. Nanayakkara, A. Pallottini, R. Schneider, L. Sommovigo, M. Topping, P. van der Werf, H. Algera, L. Barrufet, A. Hygate, I. Labbé, D. Riechers, and J. Witstok. Reionization era bright emission line survey: Selection and characterization of luminous interstellar medium reservoirs in the z gt; 6.5 universe. *The Astrophysical Journal*, 931(2):160, jun 2022.

[26] Francesco Ziparo, Andrea Ferrara, Laura Sommovigo, and Mahsa Kohandel. Blue monsters. Why are JWST super-early, massive galaxies so blue? *Mon. Not. Roy. Astron. Soc.*, 520(2):2445–2450, 2023.

[27] A. Ferrara, A. Pallottini, and P. Dayal. On the stunning abundance of super-early, massive galaxies revealed by jwst. 2022.

[28] Jr. Kennicutt, Robert C. Star Formation in Galaxies Along the Hubble Sequence. , 36:189–232, January 1998.

[29] Piero Madau and Mark Dickinson. Cosmic star-formation history. *Annual Review of Astronomy and Astrophysics*, 52(1):415–486, aug 2014.

[30] G. Sun and S. R. Furlanetto. Constraints on the star formation efficiency of galaxies during the epoch of reionization. , 460(1):417–433, July 2016.

[31] Pratika Dayal, Andrea Ferrara, James S. Dunlop, and Fabio Pacucci. Essential physics of early galaxy formation. *Monthly Notices of the Royal Astronomical Society*, 445(3):2545–2557, oct 2014.

[32] Mark R. Krumholz, Todd A. Thompson, Eve C. Ostriker, and Crystal L. Martin. The observable properties of cool winds from galaxies, AGN, and star clusters - I. Theoretical framework. , 471(4):4061–4086, November 2017.

[33] J. B. Oke and J. E. Gunn. Secondary standard stars for absolute spectrophotometry. , 266:713–717, March 1983.

[34] L. Barrufet, P. A. Oesch, R. Bouwens, H. Inami, L. Sommovigo, H. Algera, E. da Cunha, M. Aravena, P. Dayal, A. Ferrara, Y. Fudamoto, V. Gonzalez, L. Graziani, A. Hygate, I. de Looze, T. Nanayakkara, A. Pallottini, R. Schneider, M. Stefanon, M. Topping, and P. van Der Werf. The alma rebels survey: The first infrared luminosity function measurement at $\mathbf{z \sim 7}$, 2023.

[35] Yoshiaki Ono, Masami Ouchi, Yuichi Harikane, Jun Toshikawa, Michael Rauch, Suraphong Yuma, Marcin Sawicki, Takatoshi Shibuya, Kazuhiro Shimasaku, Masamune Oguri, Chris Willott, Mohammad Akhlaghi, Masayuki Akiyama, Jean Coupon, Nobunari Kashikawa, Yutaka Komiyama, Akira Konno, Lihwai Lin, Yoshiki Matsuoka, Satoshi Miyazaki, Tohru Nagao, Kimihiko Nakajima, John Silverman, Masayuki Tanaka, Yoshiaki Taniguchi, and Shiang-Yu Wang. Great Optically Luminous Dropout Research Using Subaru HSC (GOLDRUSH). I. UV luminosity functions at z 4–7 derived with the half-million dropouts on the 100 deg2 sky†. *Publications of the Astronomical Society of Japan*, 70(SP1), 11 2017. S10.

[36] P. A. Oesch, G. Brammer, P. G. van Dokkum, G. D. Illingworth, R. J. Bouwens, I. Labbé , M. Franx, I. Momcheva, M. L. N. Ashby, G. G. Fazio, V. Gonzalez, B. Holden, D. Magee, R. E. Skelton, R. Smit, L. R. Spitler, M. Trenti, and S. P. Willner. A REMARKABLY LUMINOUS GALAXY ATiz/i= 11.1 MEASURED WITHiHUBBLE SPACE TELESCOPE/iGRISM SPECTROSCOPY. *The Astrophysical Journal*, 819(2):129, mar 2016.

[37] Lin Yan, A. Sajina, F. Loiacono, G. Lagache, M. Béthermin, A. Faisst, M. Ginolfi, O. Le Fèvre, C. Gruppioni, P. L. Capak, P. Cassata, D. Schaerer, J. D. Silverman, S. Bardelli, M. Dessauges-Zavadsky, A. Cimatti, N. P. Hathi, B. C. Lemaux, E. Ibar, G. C. Jones, Anton M. Koekemoer, P. A. Oesch, M. Talia, F. Pozzi, D. A. Riechers, L. A. M. Tasca, Sune Toft, L. Vallini, D. Vergani, G. Zamorani, and E. Zucca. The ALPINE-ALMA [C II] Survey: [C II] 158 μm Emission Line Luminosity Functions at z $\sim$ 4-6. , 905(2):147, December 2020.